Using Optical Spectroscopy to Map the Geometry and Structure of the Irradiated Accretion Discs in Low-mass X-ray Binaries: The Pilot-Study of MAXI J0637−430

B.E. Tetarenko[1]⋆, A.W. Shaw[2], E.R. Manrow[1], P.A. Charles[3], J.M. Miller[1], T.D. Russell[4], and A.J. Tetarenko[5]

[1]*Department of Astronomy, University of Michigan, 1085 South University Avenue, Ann Arbor, MI 48109, USA*
[2]*Department of Physics, University of Nevada, Reno, NV 89557, USA*
[3]*Department of Physics & Astronomy, University of Southampton, Southampton SO17 1BJ, UK*
[4]*Anton Pannekoek Institute for Astronomy, University of Amsterdam, Science Park 904, NL-1098 XH Amsterdam, The Netherlands*
[5]*East Asian Observatory, 660 N. A'ohōkū Place, University Park, Hilo, Hawaii 96720, USA*

ABSTRACT

The recurring transient outbursts in low-mass X-ray binaries (LMXBs) provide us with strong test-beds for constraining the poorly understood accretion process. While impossible to image directly, phase-resolved spectroscopy can provide a powerful diagnostic to study their highly complex, time-dependent accretion discs. We present an 8-month long multi-wavelength (UV, optical, X-ray) monitoring campaign of the new candidate black hole LMXB MAXI J0637−430 throughout its 2019/2020 outburst, using the *Neil Gehrels Swift Observatory*, as well as three quasi-simultaneous epochs of Gemini/GMOS optical spectroscopy. We find evidence for the existence of a correlation between the X-ray irradiation heating the accretion disc and the evolution of the He II 4686 Å emission line profiles detected in the optical spectra. Our results demonstrate a connection between the line emitting regions and physical properties of the X-ray irradiation heating the discs during outburst cycles of LMXBs. Further, we are able to show that changes in the physical properties of the irradiation heating the disc in outburst can be imprinted within the H/He emission line profiles themselves in these systems.

Key words: accretion — accretion discs — black hole physics — stars: individual (MAXI J0637−430) — binaries: spectroscopic — X-rays: binaries

1 INTRODUCTION

Among accreting astrophysical systems, low-mass X-ray binaries (LMXBs), containing discs of matter fed by nearby, low-mass stars flowing onto compact stellar remnants (black holes or neutron stars), provide ideal test beds for constraining the poorly understood process of accretion. Many of these systems are transient, undergoing frequently (usually timescales of ∼ years) recurrent outbursts. Thus, these systems offer the unique opportunity to study accretion over observable (day-month) timescales (Charles & Coe 2006; Remillard & McClintock 2006; Tetarenko et al. 2016).

The mechanism behind these outbursts can be broadly explained with the disc-instability model (DIM), whereby such transient behaviour is explained via the accretion disc cycling between a hot, ionized outburst state and a cool, neutral, quiescent state. This limit-cycle, triggered by the accumulation of matter in the disc as a result of mass-transfer from the companion star, heats the disc until a significant portion is ionized. The viscosity of the disc (i.e. ability to move angular momentum outwards) increases dramatically when it is in this ionized state. This results in a rapid in-fall of matter onto the compact object, and in-turn a bright outburst. For a recent review of the DIM see Hameury (2020).

While we can image their supermassive relatives (i.e., Event Horizon Telescope (EHT); Event Horizon Telescope Collaboration et al. 2019), LMXBs are far too small and distant to be imaged directly. However, phase-resolved spectroscopy can provide an alternative diagnostic to study their highly complex, time-dependent accretion discs. The spectral signature of an LMXB is detection of strong H and He emission lines at optical wavelengths (Hα, Hβ, He I, He II; e.g., Dubus et al. 2001b; Casares 2015) from the accretion disc (Charles & Coe 2006). These "accretion signatures" typically show a double-peaked profile, due to Doppler motions in the binary (Crawford & Kraft 1956; Casares 2015), with the line profile shape depending on the distribution of emission over the disc surface. As a result, these emission line profiles encode within them a projection of the disc itself along the line of sight. As the spatial distribution of line emission is a tracer of structure in the disc, these emission

⋆ E-mail: btetaren@umich.edu

lines can, in principle, be used to effectively describe how matter in the disc behaves and evolves over time (e.g., Marsh 2001, 2005).

LMXBs harbouring stellar-mass black holes (BH-LMXBs), are of particular interest. Most of the optical light emitted by their accretion discs comes from reprocessed X-rays, arising close to the black hole, heating the outer disc (van Paradijs & McClintock 1994; van Paradijs 1996). This X-ray irradiation is the dominant factor that determines the temperature over most of the disc during outburst. By illuminating the disc surface, irradiation controls the outburst decay from peak to quiescence. Consequently, the light-curve profile for an outbursting irradiated disc, as predicted by the disc-instability model (DIM), can be characterized into multiple stages (Dubus et al. 1999, 2001a), defined by how (and on what timescale) matter moves through the disc itself.

A combination of the (i) first stage after the outburst peak, the viscous decay, and (ii) subsequent transition to the second, irradiation-controlled stage of the decay, together offer the ideal means to study both the source of the irradiation and its effect on the disc. During the viscous stage of the decay, X-ray irradiation is at its strongest and thus, the entire disc is thought to be in a hot, ionized state. At this point, the rate of mass-accretion onto the black hole ($\dot{M}_{in}$) is much greater than the rate of mass-transfer from the companion to the disc ($\dot{M}_{tr}$). Thus, mass in the disc is assumed to change only through viscous accretion, leading to the characteristic "exponential" light-curve decay profile shape. The transition to the second, irradiation-controlled decay stage occurs as a result of the temperature dropping in the outer disc regions, and subsequent formation and propagation of an inward moving cooling front at a speed determined by the strength of the decaying X-ray irradiating flux (Dubus et al. 2001a; Tetarenko et al. 2018b,a). Both of these accretion regimes, to date, have not yet been well studied in LMXBs. Recently, Tetarenko et al. (2018b,a) developed a methodology to characterize observed LMXB light-curves based on the predictions of the DIM. Together, with multi-wavelength capabilities and rapid-response times of the instruments aboard the Neil Gehrels *Swift* Observatory, their analytical models allow one to track and predict the evolution of an LMXB on daily timescales during an outburst.

Despite decades of effort, the radial profile and geometry of the irradiation source heating LMXB discs are not well understood (Dubus et al. 1999, 2001a; Vrtilek et al. 1990; King et al. 1996; Reynolds & Miller 2013; Rykoff et al. 2007; Degenaar et al. 2014). As the irradiation is only important in the outer regions (typically greater than hundreds of gravitational radii) of LMXB discs, H/He emission lines are an ideal means to probe it. In this work, we combine X-ray, optical, and ultraviolet spectral and photometric data from *Swift*, modern Doppler tomography techniques (e.g., Steeghs 2003), and the H/He disc emission lines detected in Gemini Multi-Object Spectrograph (GMOS) optical spectra. With these data we attempt to map the illumination pattern of the irradiation heating a transient BH-LMXB disc during both the viscous stage and transition to the irradiation-controlled stage of an outburst decay. Specifically, these data have allowed us to track and quantify how variations in this irradiation-heating over an outburst affect the physical properties of the disc through its emission line profiles. This is a first (and crucial) step to developing a method to use phase-resolved spectroscopy to effectively probe the geometry/structure of the gas making up an outbursting BH-LMXB accretion disc, which has not been done before.

This paper is organized as follows: Section 2 outlines the details of the 2019/2020 outburst of new candidate BH-LMXB MAXI J0637−430. Section 3 discusses the multi-wavelength ob-

servational data used in this work. Section 4 discusses the multi-wavelength (X-ray, optical and UV) spectral and time-series analysis done on MAXI J0637−430. In Section 5 we discuss the relationship found between irradiation-heating and disc emission line profiles for this source and the implications such a finding has for LMXBs in general. Finally in Section 6 we summarize this work.

2   GALACTIC BH-LMXB CANDIDATE: MAXI J0637−430

2.1   Discovery and Multi-wavelength Outburst Monitoring

MAXI J0637−430 (hereafter J0637), a newly discovered candidate BH-LMXB, was first detected in outburst by the *Monitor of All-sky X-ray Image* (*MAXI*; Matsuoka et al. 2009) on 2019 November 02 (Negoro et al. 2019). Follow-up observations with the X-ray Telescope (XRT; Burrows et al. 2005) aboard *Swift* (2019 November 03; Kennea et al. 2019) and the *Nuclear Spectroscopic Telescope Array* (*NuSTAR*; Harrison et al. 2013 - 2019 November 05; Tomsick et al. 2019) showed a soft X-ray spectrum, well fit by an absorbed power-law + disc blackbody model. In addition, a bright optical counterpart with a position not coincident with any known star, was also detected by the Ultraviolet and Optical Telescope (UVOT; Roming et al. 2005) aboard *Swift* inside the X-ray error circle. Both X-ray and optical observations were highly suggestive of an outbursting X-ray binary in the soft accretion state, and furthermore the X-ray spectral shape favours a BH over a neutron star as the compact object.

Further, optical spectral observations, taken on 2019 November 03 with the Southern Astrophysical Research (SOAR) telescope (Strader et al. 2019), revealed strong, broad, double-peaked Hα, and He II 4686 Å emission at Galactic velocities, and weaker Hβ, Hγ, and He I 5875 Å and 6678 Å emission as well, providing strong evidence for J0637 being a new, candidate BH-LMXB in outburst.

J0637, first localized by *Swift*, was also later detected in the radio band by the Australia Telescope Compact Array (ATCA; at frequencies of 5.5 and 9 GHz) on 2019 November 06 (Russell et al. 2019b), giving a refined position of: RA, Dec (J2000) = $06^h36^m23^s7 \pm 0\farcs2$, $-42°52'04\farcs1 \pm 0\farcs7$. At this position, with a galactic latitude of −20 degrees, the interstellar reddening is low, making J0637 a great target for both blue and red time-resolved spectroscopy.

Radio flux densities were consistent with emission arising from a discrete ejection event (e.g., steep spectrum; Russell et al. 2019a), expected if J0637 was an outbursting BH-LMXB in a soft or soft-intermediate accretion state. A second radio epoch was taken on 2020 January 8 (as analyzed in this work), where J0637 was not detected in either the 5.5 or 9 GHz band. See Figure 1 for the radio light-curve and Section 3.3 for a detailed discussion.

Monitoring on approximately daily timescales with both *Swift* (this work; Figure 1) and the *Neutron star Interior Composition Explorer* (*NICER*; Remillard et al. 2020) showed that J0637 remained in a soft accretion state for approximately 70 days, before beginning the transition back to the hard accretion state between 2020 January 12-14 (MJD 58860-58862). After the state transition occurred (approximately 2020 January 29; MJD 58877), J0637 then began its final decay toward quiescence. This decay, lasting approximately 4 months, was observed at both X-ray and optical wavelengths by *Swift* XRT and UVOT (this work) and the Faulkes telescopes at the Las Cumbres Observatory (as part of the XB-NEWS Monitoring Program; Johar et al. 2020). J0637 was thought to likely reach a quiescent level in 2020 June (Tomsick & Lazar 2020).
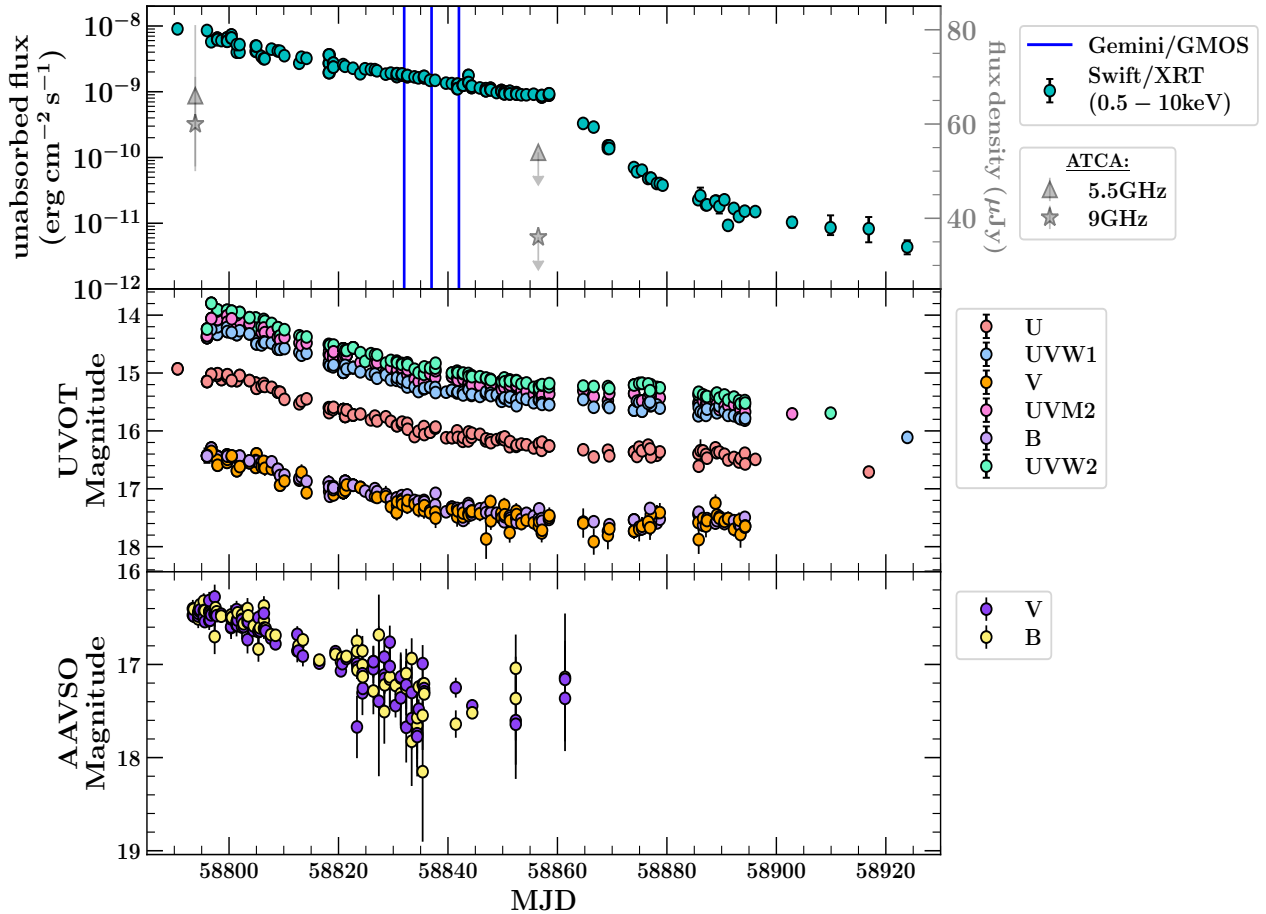
Figure 1. Multi-wavelength light-curve showing the evolution of the 2019/2020 outburst of J0637: *(top) Swift*/XRT ($0.5 - 10$ keV), *(middle) Swift*/UVOT, and *(bottom)* AAVSO. UVOT and AAVSO magnitudes have not been de-reddened. The grey data points and grey right-side axis in the *top* panel show the two epochs of radio (5.5 and 9 GHz) data taken with ATCA. The vertical solid blue lines in the *top* panel show the three days in which Gemini/GMOS spectra were obtained.

2.2 Binary Orbital Parameters

While an optical counterpart was detected during outburst (Kennea et al. 2019), little is known about the orbital parameters of J0637. Thus, in this work, following Tetarenko et al. (2018a), we sample a BH mass (M_{BH}) and binary mass ratio (q) from the Galactic distributions of Özel et al. (2010) and Tetarenko et al. (2016), respectively, and assume a broad, uniform distribution in distance of $d = 5 - 15$ kpc.

Lastly, we attempted to constrain the binary orbital period using a combination of (i) a broad-band spectral energy distribution (SED) fitting method (see Section 4.1), with data from our continuous *Swift* (XRT+UVOT) monitoring (see Section 3.1 and Figure 1), and (ii) the detection of Hydrogen emission in the optical spectrum. The SED fitting method provides an upper limit of $P_{orb} \lesssim 4$ hrs. While the detection of Hα emission in the optical spectrum (See Section 4.4 and Figure 2) rules out ultra-compact systems ($P_{orb} \lesssim 1.5$ hrs). Thus, we assume an orbital period of $P_{orb} = 2 - 4$ hrs. This would make it one of the shortest in this class of objects.

We note that while many light-curves of LMXBs in outbursts exhibit periodicities known as "superhumps", resulting from a precessing accretion disc, with a period typically close to the true P_{orb} of the binary system (e.g., see Zurita et al. 2008; Patterson et al. 2018), no evidence for periodicity was found in the publicly avail-

able AAVSO data of J0637 (see Section 3.4.1 and Hambsch et al. 2019). The available UVOT data (Section 3.1.2) lacks the cadence required to perform such an analysis.

3 OBSERVATIONS AND DATA REDUCTION

3.1 *Swift*

A total of 105 *Swift* observations were obtained from the High Energy Astrophysics Science Archive Research Center (HEASARC) Archive[1], between 2019 November 03 and 2020 March 15 (ObsId: 00012168001-00012172094; as part of University of Michigan GTO time - co-PIs: Tetarenko and Miller), covering the 2019/2020 X-ray outburst of J0637 (Figure 1). The majority of the XRT observations were taken in windowed timing (WT) mode, with a few taken in photon counting (PC) mode, when the source count rate was low. The majority of the UVOT observations were obtained in all six filters, from the UV through optical (UVW2, UVM2, UVW1, U, B, V).

---

[1] https://heasarc.gsfc.nasa.gov/docs/archive.html

3.1.1 XRT

Data were first processed with the `xrtpipeline` task from the HEASOFT v6.26 software package. In WT mode, source and background spectra were extracted using circular apertures with a radius of 20 pixels. In PC mode, source spectra were first extracted using the same size aperature as WT mode, to determine if photon pile-up was significant. If the average count rate was greater than 0.5 counts/s, spectra were re-extracted, this time using an annular region with a 20 pixel outer radius. The radius of the central portion of the point spread function (PSF) excluded here was calculated with the `ximage` package[2] in each case. The background spectra of PC mode observations were extracted using an annulus, with inner and outer radii of 50 and 70 pixels, centered on the source.

Source and background spectra were then grouped such that each energy bin contained a minimum of 5 counts. Lastly, the response matrix files were obtained from the HEASARC calibration data base (CALDB) and the `xrtmkarf` task was used to generate ancillary response files.

XSPEC v12.10.1f (Arnaud 1996) was used to perform all of the X-ray (XRT) spectral fits in the 0.5−10 keV band. The `tbabs` model, utilizing abundances from Wilms et al. (2000), and photoionization cross-sections from Verner et al. (1996), was used to account for interstellar absorption in all fits. The hydrogen column was not well constrained in the XRT spectra, and thus was fixed at $N_H = 4.39 \times 10^{20}$ cm^{-2} (corresponding to $E(B-V) = 0.064$; see Section 3.1.2) for all fits (Güver & Özel 2009). Note that, HI4PI[3] find a Galactic N_H in the direction of the source ($N_H = 5.23 \times 10^{20}$ cm^{-2}) to be similar to our estimate. Further, using the equivalent width of the NaD (I/S) absorption line present in the Gemini/GMOS optical spectra (Figure 2) yields an $E(B-V) = 0.068^{+0.009}_{-0.008}$ (see e.g., Munari & Zwitter 1997), consistent with the reddening estimate we use in this work.

3.1.2 UVOT

UVOT, a 30 cm diameter telescope, operates simultaneously with XRT. Thus, we have a total of 105 UVOT observations simultaneous with the XRT exposures described above, 100 of which contain exposures in multiple UVOT filters.

Using the HEASOFT task `uvotsource`, aperture photometry was performed on all UVOT images, using a circular region centred on the source with a radius of 5″. The background circular region used measured 20″ in radius and was centered in a source free region. All magnitudes were computed in the Vega system, with the known flux zero-points for each filter used to convert to flux densities. Uncertainties in UVOT magnitudes/flux densities include a combination of the statistical error (1σ confidence level) and systematic uncertainty used to account for error in the shape of the PSF. Photometric UVOT data was corrected for interstellar extinction according to Fitzpatrick & Massa (1999). To deredden these data, the `specutils` package in PYTHON was used, with an $E(B-V) = 0.064$ (Strader et al. 2019).

UVOT spectra were extracted in each available filter using the `uvot2pha` task, source and background regions as described above, and the response matrices available for each filter from HEASARC CALDB. If necessary, the `uvotimsum` task was used first to co-add individual image extensions, creating one image per

filter, before spectra were extracted. XSPEC v12.10.0c (Arnaud 1996) was used to perform all of the broad-band (XRT+UVOT) spectral fits. The `redden` model, with an $E(B-V)$ fixed at a value of 0.064, was used to account for extinction in all fits.

3.2 Gemini/GMOS

On 2019 December 8, we triggered our Gemini/GMOS-South Target-of-Opportunity (ToO) programme (GS-2019B-Q-233; PI Tetarenko) on J0637. We subsequently obtained long-slit optical spectra over three nights: 2019 December 15 (05:15:42.2334−07:14:22.1334 UT), 2019 December 20 (04:09:12.3834−06:07:45.1500 UT), and 2019 December 25 (03:30:53.8167−07:08:48.9500 UT), for a total of 42×600s individual exposures (7hrs on source). See Table A1 in Appendix A and Figure 1 for details. All data were obtained with the B600 grating, a central $\lambda = 560$nm, and a 1″ slit, with a typical resolution of 4.5-5Å.

Data were reduced using PYRAF v2.1.15 and the available Gemini/GMOS long-slit reduction cookbook[4]. First, bias residual and flat-field MasterCal reference files were created with the `gbias` and `gflat` tasks, and then used to calibrate the science exposures. Next, a bad pixel mask was created using the provided IRAF scripts[5]. Then, cosmic-ray rejection was performed on individual calibrated science exposures using the `gemcrspec` task. This task makes use of the LA-Cosmic program (van Dokkum 2001), and the provided IRAF scripts[6]. Next, basic reductions were performed and the bad pixel mask was applied to the calibrated science exposures using the `gsreduce` task. The same procedure used for the science exposures, as outlined above, was then applied to the standard star (LTT1788) exposures.

Next, arc exposures were reduced and wavelength solutions were found via the `gswavelength` task. Then, the wavelength calibration was applied (via the `gstransform` task), and sky subtraction was performed (via the `gsskysub` task), on the calibrated, cleaned, science and standard star exposures. Spectra were then extracted from individual, calibrated, cleaned, science and standard star exposures, using the `gsextract` task. Finally, daily averaged spectra were also created from the individual extracted science spectra, on each of the three days data was taken, using the `scombine` task in IRAF. Flux-calibrated spectra, summed over the three days of data taken, can be found in Figure 2.

3.3 ATCA

MAXI J0637−430 was observed by the Australia Telescope Compact Array (ATCA) on 2019-11-06 (17:23 − 19:55 UT) and 2020-01-05 (12:16 − 14:13 UT). The observations were recorded simultaneously at central frequencies of 5.5 and 9 GHz, with 2048 MHz of bandwidth at each central frequency (2048 × 1 MHz channels). For both observations PKS 1934−630 was used for primary flux calibration and PKS 0629−418 was used for secondary phase calibration. Following standard procedures within the Common Astronomy Software Application (CASA, version 5.1.0; McMullin et al. 2007[7]), the data were first edited for radio frequency interference

---

[2] http://www.swift.ac.uk/analysis/xrt/pileup.php
[3] https://heasarc.gsfc.nasa.gov/cgi-bin/Tools/w3nh/w3nh.pl
[4] http://ast.noao.edu/sites/default/files/GMOS_Cookbook/
[5] https://gmos-data-reduction-problems-and-solutions. readthedocs.io/en/latest/appendix.html
[6] http://ast.noao.edu/sites/default/files/GMOS_Cookbook/ GettingStarted.html
[7] https://casaguides.nrao.edu/index.php?title=Main_Page
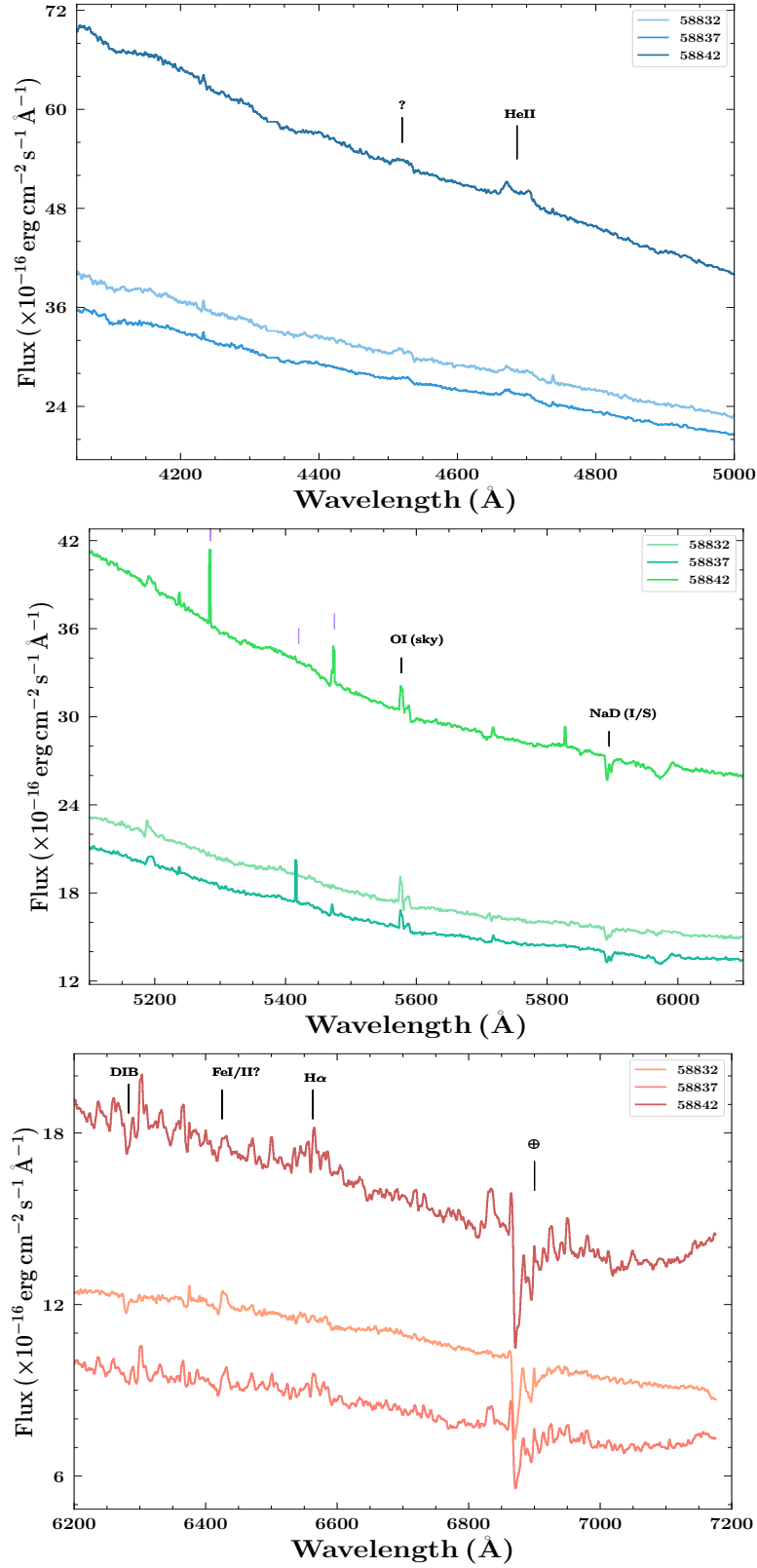
Figure 2. Flux-calibrated Gemini/GMOS optical spectra of J0637, summed over each of the three days during which data was taken: 2019 December 15 (MJD 58832), 2019 December 20 (MJD 58837), and 2019 December 25 (MJD 58842). The two strongest disc emission lines (He II 4686 Å and Hα), interstellar absorption lines (I/S), diffuse interstellar bands (DIB), telluric absorption lines (⊕), and poorly-subtracted night-sky emission lines (sky) are marked in black. Purple lines mark narrow emission features that are not real and ? signifies unknown features (see Section 4.4 for discussion).

(RFI), before being calibrated and then imaged. For the 2019-11-06 observation, imaging used a Briggs robust parameter of 0, balancing sensitivity and resolution, providing synthesised beams of $9.3'' \times 1.1''$ at 5.5 GHz and $6.0'' \times 0.7''$ at 9 GHz with a position angle of 10 degrees East of North for both frequencies. For our 2020-01-05 ATCA observation, we imaged with a Briggs robust parameter of 2 to maximise the sensitivity, providing synthesised beams of $22.4'' \times 1.8''$ at 5.5 GHz and $12.8'' \times 1.1''$ at 9 GHz, both with positions angle of 2 degrees West of North.

The radio counterpart to MAXI J0637−430 was detected during our 2019-11-06 ATCA observations, but not on 2020-01-05. On 2019-11-06 we fitted for a point source in the image plane by applying a Gaussian with the full width at half maximum fixed to the synthesised beam parameters. Doing so, we measured flux densities of 66±15 μJy at 5.5 GHz and 60±10 μJy at 9 GHz. On 2020-01-05, we did not detect radio emission associated with the target, with 3σ radio upper-limits of 54 μJy/beam at 5.5 GHz and 36 μJy/beam at 9 GHz. Stacking the two bands together provides a 3σ upper-limit of 30 μJy/beam (at a central frequency of 7.25 GHz).

3.4 AAVSO

Publicly available observations of J0637, in the V and B bands (Vega magnitudes), were obtained from the AAVSO International Database[8]. See Figure 1 for the light-curves.

3.4.1 Search For Periodicity

To search for periodicities in the optical/UV data we used the Lomb-Scargle periodogram implemented in the `astropy` package (Astropy Collaboration et al. 2013; Price-Whelan et al. 2018) in PYTHON (Lomb 1976; Scargle 1982; Zechmeister & Kürster 2009). This tool is ideal for detecting periodic signals in unevenly sampled data. We do not detect any significant (99% significance level) periodicities in the data on timescales < 100 days (i.e., length of the sampled light curves). Note that, we have also checked the equivalent width (EW) light-curves of the He II 4686 Å emission line detected in the GMOS spectra (see 4.4). Again, no significant periodicities were found.

4 RESULTS

4.1 Spectral Fitting

4.1.1 X-ray (XRT)

All X-ray spectra were adequately fit (via the χ^2 statistic), in the 0.5 − 10 keV band, with either an absorbed power-law (`tbabs*cflux*powerlaw`), absorbed disc-blackbody (`tbabs*cflux*diskbb`), or combination power-law + disc blackbody (`tbabs*cflux*(diskbb+powerlaw)`) model in XSPEC. `cflux` is convolution model used to to compute the flux of different spectral components. Used as it is here, with the normalization of either the `diskbb` or `powerlaw` model components fixed to a non-zero value, a flux estimate for the entire spectral model is the output. See Figure 1 and Table B1 in Appendix B for the best-fit model parameters, along with the resulting 0.5 − 10 keV fluxes, for each *Swift* epoch.

4.1.2 Broad-band (XRT+UVOT)

Of the 100 *Swift* epochs, for which there are multiple UVOT filters, we attempted to fit the broad-band (XRT+UVOT) spectrum with the `redden*diskir` model in XPSEC. Adequate fits were obtained for 80 of these observations, covering the time-period: 58795 − 58866.

`diskir` (Gierliński et al. 2009) models an irradiated accretion disc using a total of 9 parameters[9]. During each epoch, we fit for the following 5 parameters: disc normalization (N_{disc}), inner disc temperature (T_{in}), log of the ratio between outer and inner disc radius (logrout), fraction of bolometric flux thermalized in the outer disc region (f_{out}), and ratio of luminosity in the Compton tail to the un-illuminated disc (L_c/L_d). In addition, we fixed the remaining four parameters to typical values expected for LMXBs: power-law photon index ($\gamma = 1.7$), electron temperature ($T_e = 100$ keV), fraction of the luminosity in the Compton tail thermalized in the inner disc ($f_{in} = 0.1$), and the radius of the Compton illuminated disc as a fraction of the inner disc radius ($r_{irr} = 1.2$). See Figure C1 in Appendix C for example SEDs, quasi-simultaneous (within at most 10 hrs) with the epochs where Gemini/GMOS and ATCA data were taken. See Table B2 in Appendix B for best-fit model parameters.

The best-fit `diskir` parameters obtained could then be used to estimate the following physical parameters of the irradiated accretion disc in J0637: outer disc radius (R_{out}), inner disc radius (R_{in}), mass-accretion rate onto the BH ($\dot{M}_{BH}$), and the fraction of X-ray flux intercepted and reprocessed in the outer disc (C). See Figure 3.

The inner and outer disc radius are computed as follows, assuming a distance of $d = U(5, 15)$ kpc and an inclination averaged over all angles:

$$R_{out} = R_{in} 10^{logrout}, \tag{1}$$

where,

$$R_{in} = 1 \times 10^5 \left(\frac{d}{10\mathrm{kpc}} \right) \left(\frac{N_{disc}}{\cos i} \right)^{1/2}. \tag{2}$$

Here the disc normalization term, N_{disc}, is defined in the same way as the `diskbb` model[10] in XSPEC.

Using the resulting R_{out} estimates, computed from the broad-band spectral energy distribution (SED) fits during the viscous decay stage (when the whole disc is thought ot be in a hot, ionized state), we can estimate the orbital period (P_{orb}) of J0637. Using typical binary orbital parameters of BH-LMXBs (see Section 2.2 and Tetarenko et al. 2016), we find a $P_{orb} \lesssim 4$ hrs (see Figure 3).

For a situation in which the outer part of an LMXB accretion disc is irradiated by a central X-ray source, the temperature profile of the (assumed steady-state) disc can be written as a combination of viscous (Frank et al. 2002) and irradiated (Dubus et al. 1999) portions such that,

$$T_{eff}^4(R) = T_{visc}^4(R) + T_{irr}^4(R), \tag{3}$$

where,

$$T_{visc}^4 = \frac{3GM_1\dot{M}_{BH}}{8\pi\sigma R^3} \left[1 - \left(\frac{R_{in}}{R} \right)^{1/2} \right], \tag{4}$$
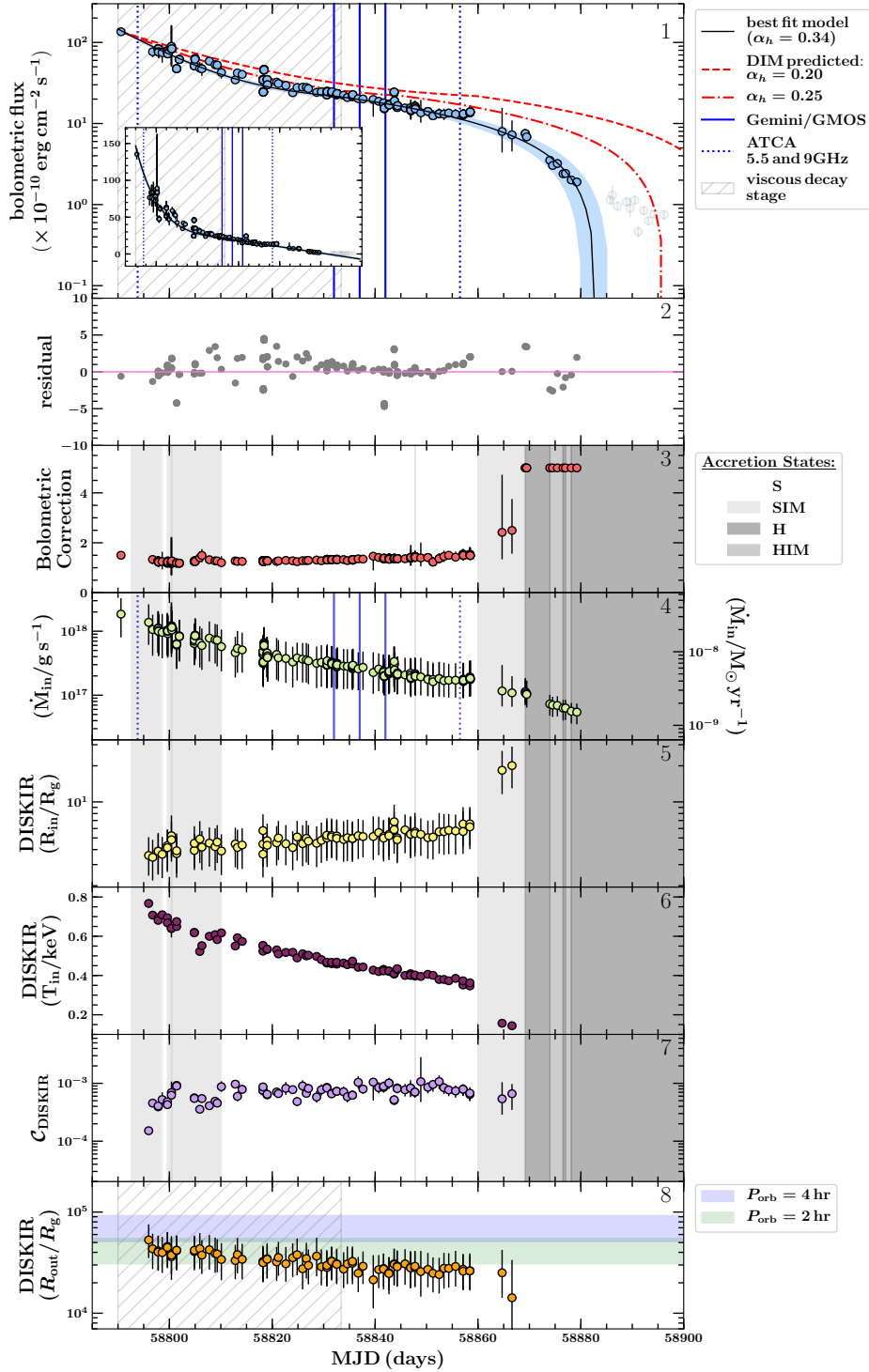
Figure 3. *(top panel)* the bolometric light-curve for the 2019/2020 outburst of J0637 fit with the analytical DIM models from Tetarenko et al. (2018b,a). The best-fit (solid black line) and 1σ confidence interval on the fit (blue shaded region) are shown. The timescale of the viscous stage of the decay (grey cross hatch region) corresponds to an alpha-viscosity parameter of α_h=0.34. Also shown are model light-curve decay profiles corresponding to an α_h=0.2 and α_h=0.25, to demonstrate how light-curve profile shape changes with alpha-viscosity. The inset axis shows the data in linear space. The epochs in which Gemini/GMOS (solid blue lines) and ATCA (dotted blue lines) data were taken are also displayed. *(second panel)* residuals on the light-curve fit. *(third panel)* and *(fourth panel)*: the bolometric corrections, computed from a combination of *Swift* band-limited X-ray and broad-band (XRT+UVOT) spectral fitting, and central mass-accretion rate, over time, respectively. *(fifth panel)* through *(bottom panel)*: the inner disc radius R_{in} (in units of R_g, assuming an $M_1 = N(7.8, 1.2) M_\odot$), inner disc temperature T_{in} (in keV), reprocessed X-ray fraction (C_{DISKIR}), and outer disc radius R_{out} (also in units of R_g), computed from the broad-band (XRT+UVOT) spectral fitting (see Section 4.1.2). The estimated R_{out}, corresponding to a P_{orb} = 2 hr (green shaded region) and P_{orb} = 4 hr (blue shaded region), calculated by sampling M_1 and q from the observational Galactic distributions (see Section 2.2) are also shown in the *(bottom panel)*. Both C_{DISKIR} *(seventh panel)* and R_{out} *(bottom panel)* are computed assuming an average over all inclination angles. Lastly, the *(third panel)* through *(seventh panel)* also display the accretion state evolution of J0637, computed from the *Swift* data (see Section 4.1.4), in various shades of grey. See legend on the plot.
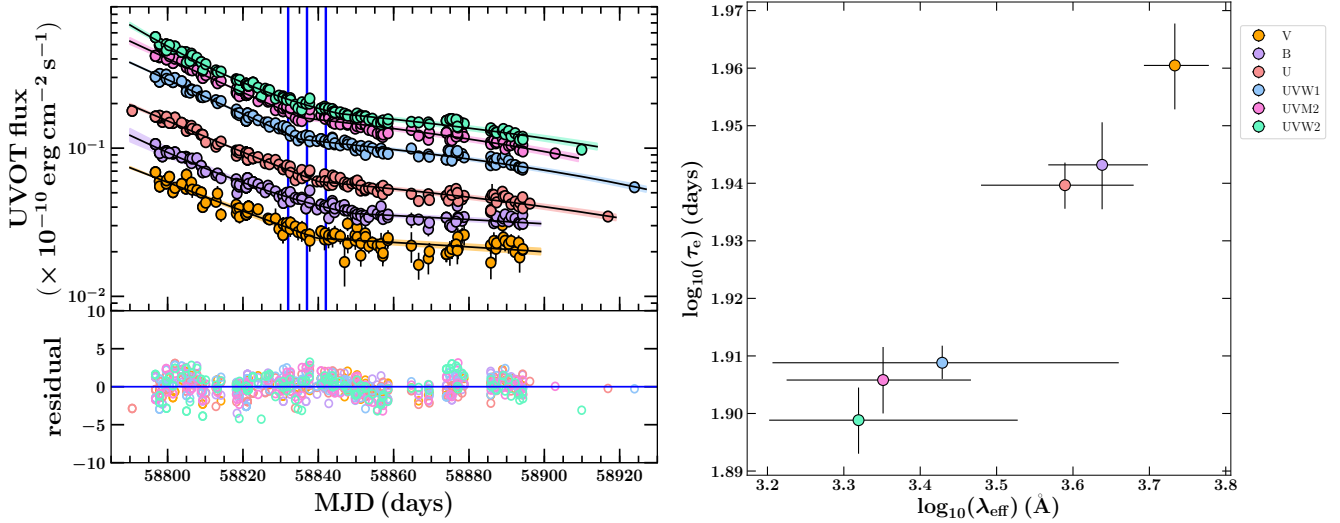
Figure 4. *(left panel)* individual band-pass *Swift*/UVOT light-curves, during the 2019/2020 outburst of J0637, fit with the analytical DIM models from Tetarenko et al. (2018b,a). The best-fit and 1σ confidence interval on the fit, for each band-pass, are displayed as solid black lines and shaded coloured regions, respectively. Also shown are the epochs in which Gemini/GMOS data were taken (solid blue lines). Residuals of each fit are displayed in the lower panel. *(right panel)* correlation between exponential (viscous) decay timescale (τ_e) and effective wavelength ($\lambda_{\rm eff}$) for all six UVOT band-passes. The uncertainty on wavelength is the band-pass limits of each filter.

and,

$$T_{\rm irr}^4 = C \frac{\dot{M}_{\rm BH} c^2}{4\pi\sigma R^2}. \tag{5}$$

One can write the reprocessed fraction, C (as defined above), in terms of `diskir` parameters, as follows (see Meshcheryakov et al. 2018 for details):

$$C = \eta\sigma f_{\rm out} F_{\rm bol}^{-1} \left(\frac{R_{\rm in}}{\rm cm}\right)^2 \left(\frac{T_{\rm in}}{K}\right)^4 \left(\frac{d}{\rm cm}\right)^{-2}, \tag{6}$$

where $F_{\rm bol}$ is the bolometric flux, obtained by integrating over the best-fit broad-band SED, and η is the accretion efficiency defined as in Coriat et al. (2012),

$$\eta = \begin{cases} 0.1\left(\frac{\dot{M}}{0.01\dot{M}_{\rm edd}}\right) & L_X < 0.01 L_{\rm edd} \\ 0.1 & L_X \geq 0.01 L_{\rm edd}, \end{cases}$$

where the Eddington accretion rate is $L_{\rm edd} = 0.1\dot{M}_{\rm edd}c^2$.

Lastly, bolometric flux, $F_{\rm bol}$, can then be converted to an observed $\dot{M}_{\rm BH}$ via,

$$\dot{M}_{\rm BH} = \frac{F_{\rm bol}(4\pi d^2)}{\eta c^2}. \tag{7}$$

4.1.3 Bolometric Correction

The calculated $F_{\rm bol}$, in combination with the band-limited ($0.5-10$ keV) X-ray flux (F_X; see Section 4.1.1), were used to compute a bolometric correction for each *Swift* epoch. For (i) the first *Swift* epoch (MJD 58790), in which only data from the UVOT/U filter was available, and (ii) late in the decay (post-58866), where we were unable to obtain adequate fits to the broad-band SED, standard bolometric corrections valid for LMXBs, estimated for each accretion state by Migliari & Fender (2006), were assumed. See Figure 3.

4.1.4 Accretion States

We classify observations of J0637 into four spectral accretion states: hard (H), hard-intermediate (HIM), soft-intermediate (SIM) and soft (S), as defined in Marcel et al. (2019). Their state classification is based on two spectral signatures: the power-law fraction (PLf), defined as the ratio of the power-law flux to the total flux, and the photon index, γ. Here the PLf is computed using the best-fit to the XRT spectra (Section 4.1.1), bolometric corrections (Section 4.1.4), and $F_{\rm bol}$ (Section 4.1.2), for each *Swift* epoch. See Figure 3.

4.2 Light-curve Fitting

4.2.1 Bolometric Light-curve

We have applied the Bayesian methodology of Tetarenko et al. (2018b,a), fitting the bolometric light-curve of J0637 with their analytical DIM models. We find the decay profile for the 2019/2020 outburst of J0637 to be well fit with the exponential + linear shaped decay profile, as is commonly found across the Galactic BH-LMXB population (Tetarenko et al. 2018b). The best-fit, as shown in Figure 3, gives an exponential (viscous) time-scale of $\tau_e = 52.9^{+0.8}_{-0.9}$ d, a linear decay time-scale of $\tau_l = 50.9^{+1.4}_{-1.3}$ d, and a transition (between viscous and irradiation-controlled stages) occurring at time (MJD) $t_{\rm break} = 58832.1 \pm 1.3$ and flux level of $f_t = (21.8 \pm 0.5) \times 10^{-10}$ erg cm^{-2} s^{-1}.

This best-fit profile corresponds to an: (i) alpha-viscosity parameter of $\alpha_h = 0.34^{+0.06}_{-0.05}$ in the disc, and outburst-average reprocessed X-ray fraction of $C = (9.5^{+11.2}_{-5.6}) \times 10^{-4}$, for an assumed $d = U(5, 15)$ kpc.

Interestingly, τ_e and τ_l are comparable in the decay of J0637 as predicted by the DIM (King & Ritter 1998). While this type of behaviour has also been seen in some short-$P_{\rm orb}$ Galactic BH-LMXBs (e.g., SwiftJ1357.2−0933), in the majority of the Galactic BH-LMXB population, these decay timescales have generally been found to differ significantly (Tetarenko et al. 2018a).

4.2.2 Multi-band UVOT Light-curves

In addition, we have also fit the UVOT light-curves with these analytical DIM models, for the purpose of comparing decay timescales as measured in different wavelengths bands. Figure 4 shows both the best-fit models for each UVOT band-pass and the correlation between exponential (viscous) decay timescale and effective wavelength for all six UVOT band-passes.

Fitting the data in logspace, with a Bayesian Markov Chain Monte-Carlo algorithm (see Tetarenko et al. 2020 for full details on this method), we find a clear power-law correlation of the form: $\tau_e = N_{\rm pl}\lambda_{\rm eff}^\beta$, where the exponential (viscous) decay becomes faster as wavelength decreases. The best-fit correlation yields a slope of $\beta = 0.13^{+0.04}_{-0.03}$ and a normalization of $N_{\rm pl} = 30.31^{+9.05}_{-8.94}$ for τ_e and $\lambda_{\rm eff}$ in units of days and angstroms, respectively. Interestingly, such a trend is also observed in synthetic model light-curves of LMXBs (see e.g., Dubus et al. 2001a).

4.3 Time-series Evolution of the X-ray Irradiating Source

Recently, Tetarenko et al. (2020) developed a methodology that uses multi-wavelength time-series data to track how properties of the X-ray irradiation heating the discs in LMXB systems evolve over time (on daily to weekly timescales). We have applied their methodology to the X-ray (*Swift*/XRT), and optical/UV (*Swift*/UVOT) data available for J0637 (see Section 3.1).

In doing so, we have been able to derive the time-series evolution of (i) the fraction of X-ray intercepted and reprocessed in the outer disc $C(t)$, and (ii) the temperature of the irradiation in the outer disc regions $T_{\rm irr}(t)$, throughout the 2019/2020 outburst cycle of J0637, from the light-curve data alone.

Figure 5 displays $C(t)$ and $T_{\rm irr}(t)$ compared to the irradiation properties derived from the broad-band (XRT+UVOT) SED fitting of the available *Swift* spectral data (see Section 4.1.2). We find that (i) the mid-UV (UVM2,UVW2) UVOT bandpasses best trace the irradiated disc, and (ii) a deviation of, at most, a factor of $2-3$ between the far-UV light-curve and broad-band SED derived C, well within the expected uncertainty of the Tetarenko et al. (2020) method.

Interestingly, the outburst-averaged C, derived from the bolometric light-curve profile (Section 4.2.1), remains consistent with both irradiation properties derived from the broad-band SED fitting (Section 4.1.2) and the multi-wavelength outburst light-curves (this Section). It is also worth noting that the largest deviation between these three methods occurs during the period in which the source remained in the soft accretion state.

4.4 Emission Line Analysis

The optical spectrum of J0637 is typical of what is expected for an LMXB accretion disc, with the only prominent features present being the strong double-peaked He II 4686 Å emission lines and weak, broad features, that have a wavelength consistent with Hα emission. . The optical spectrum bears a resemblance to that of another short-period (candidate) BH-LMXB, Swift J1753.5-0127 (e.g. Shaw et al. 2016), most notably the relatively weak Hα and lack of Hβ. We note that the apparently strong emission features at 5285 Å, 5420 Å and 5475 Å in Figure 2 are not real. This is indicated by the fact that they are very narrow compared to the He II 4686 Å and Hα emission, and are not present on all 3 nights data was taken. In addition, there is also an unknown broad emission feature at $\sim$ 4515 Å. While this may possibly be N III, there is no

sign of the C III/N III Bowen blend at 4640–50 Å. Thus, this feature remains puzzling. See the flux-calibrated spectra, summed over the three days in which data was taken, in Figure 2.

4.4.1 Deriving Line Profile Properties

For each daily-averaged spectra, we have (i) fit double gaussian line profiles to the emission lines, and (ii) computed the following emission line properties: full width half max (FWHM), equivalent width (EW), and double peak separation (DP). All analysis was done using the `specutils`[11] package in PYTHON and all uncertainties are purely statistical error only. See Table 1 and Figure 6 for results. Note that, given the complexity of the Hα region, the accuracy of any profile parameter coming from the line fitting procedure would be suspect. For this reason, we focus our emission line analysis in this work on the He II 4686 Å line only.

4.4.2 Constraints on Emission Radii

We estimate the radii within the disc from which the He lines are emitted using the method of Bernardini et al. (2016). The emission radii can be defined as,

$$\left(\frac{R_{\rm em}}{R_{\rm g}}\right) = \frac{1}{2}\left(cv_{\rm em}\sin i\right)^2, \tag{8}$$

where i is the binary inclination angle and $v_{\rm em}$ is the velocity (in km/s) at the radius $R_{\rm em}$ (in units of $R_{\rm g}$). Here $v_{\rm em}$ can be estimated by computing the half-width at zero intensity (HWZI) of the emission line in question. $R_{\rm em}$ computed using this method can be thought of as a conservative upper limit on the radii in which the He emission is coming from in the disc.

We have used the `specutils` package in PYTHON to compute the HWZI of the He II 4686 Å emission lines present in the daily-averaged spectra (see Table 1). Figure 7 displays $R_{\rm em,HeII}$ (computed using Equation 8) for a wide range of inclinations, compared to the: (i) inner disc radius ($R_{\rm in,DISKIR}$) and inner radius of the optical/UV emitting portion of the disc ($R_{\rm irr,DISKIR}$) computed from the broad-band SED fits (see Section 4.1.2 and 4.3), and (ii) estimated outer disc radius ($R_{\rm out}$) corresponding to different values of $P_{\rm orb}$. We observe that $R_{\rm em,HeII}$ moves inwards as the outburst evolves from late in the viscous decay to the irradiation controlled decay stage. Overall, this analysis rules out low-inclination angles for this source. This conclusion is consistent with the wide double-peak profile of the He II 4686 Å emission. The relationship between wide emission line profiles and higher binary inclination has been noted in other BH-LMXBs as well (see e.g., Orosz et al. 1994; Orosz & Bailyn 1995; Shaw et al. 2016).

4.5 Doppler Tomography

To date, Doppler tomography has been used to analyze complex emission line profiles from various classes of accreting binary systems during both outburst and quiescence (see e.g., Marsh 2001). Using emission line profiles observed through an entire orbit, this technique creates a projection of these emission lines in velocity space around the binary, effectively constructing an "image" of the disc on micro-arcsecond scales (see Steeghs 2004; Marsh & Horne 1988; Marsh 2001, 2005). Synonymous to a CAT-scan, which uses X-ray images, taken at different angles, to reproduce an image of
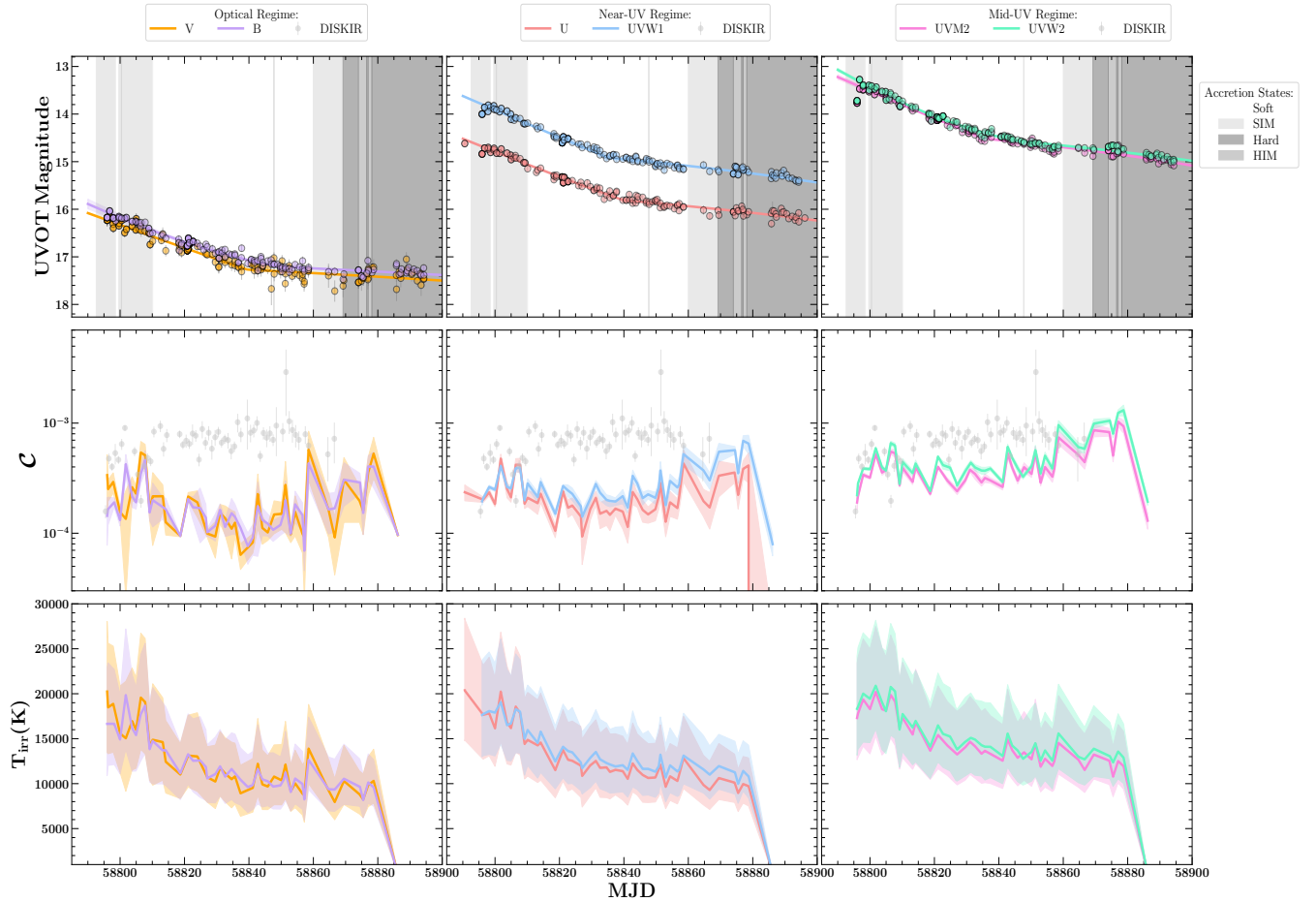
---

[11] https://specutils.readthedocs.io/en/stable/

Figure 5. X-ray irradiation properties derived from directly comparing the bolometric outburst light-curve, to the optical *(left)*, near-UV *(middle)*, and mid-UV *(right)* outburst light-curves of J0637. The *(top panels)* show dereddened *Swift*/UVOT magnitude as a function of time. The *(middle panels)* compare the fraction of X-rays intercepted and reprocessed in the outer disc as a function of time (C; solid coloured lines), calculated with the multi-wavelength light-curve method (Section 4.3), to the reprocessed fraction derived from the broad-band SED fitting (C_{DISKIR}, grey translucent data points; Section 4.1.2). The *(bottom panels)* display the irradiation temperature at the outer disc radius, T_{irr}, calculated with the multi-wavelength light-curve method. Coloured shaded regions in the *(middle panels)* and *(bottom panels)* show the 1σ confidence interval on C and T_{irr}, respectively, computed by taking into account uncertainty in X-ray flux, distance, M_{BH}, q, R_{in}, and UVOT magnitude. Shaded grey regions in the *(top panels)* show the accretion state evolution of the source over time (Section 4.1.4). See legend for details.

complex structures inside the human body, this technique uses a 2-dimensional spectral data set (i.e., time series of line profiles) to draw a velocity-resolved blueprint ("tomogram") of the line emission over the disc (Marsh 2001).

Thus, the Doppler tomography analysis technique can be used to study the structure of the disc in J0637 via orbital variation of the disc emission lines present in our Gemini/GMOS optical spectra. Accordingly, we have created doppler tomograms of the He ɪɪ 4686 Å emission (over our entire Gemini/GMOS data-set; Section 3.2) by making use of Tom Marsh's doppler[12] software package in PYTHON (see Marsh & Horne (1988) for details). Figures 8 displays the resulting He ɪɪ 4686 Å tomograms. As the system parameters of J0637 are not yet known, we have (i) created tomograms corresponding to the estimated P_{orb} range (2 − 4 hrs), and (ii) over-plotted the Roche lobe of the compact object (dashed line) and companion star (solid line) using typical binary orbital parameters of BH-LMXBs

(see Section 2.2 and Tetarenko et al. 2016): $M_1 = 7.8$, $q = 0.1$. Further, we consider both a low ($i = 5°$) binary inclination angle and an average over all inclination angles when plotting the tomograms to clearly show that it is likely J0637 does not have a very low inclination. The tomograms show He ɪɪ 4686 Å emission at large velocities. This observation is consistent with our constraints on emission radii estimated from the HWZI of each line (see Section 4.4.2).

5 DISCUSSION

5.1 The Relationship between Irradiation-heating and Disc Emission Line Profiles

It has become standard practice to use double-peaked emission lines in LMXB spectra to trace accretion disc dynamics (e.g., Casares 2015, 2016). In LMXBs, the existence of these emission lines in outburst is thought to be the result of X-ray irradiation of the disc. Thus, we have searched for the existence of a correlation between the
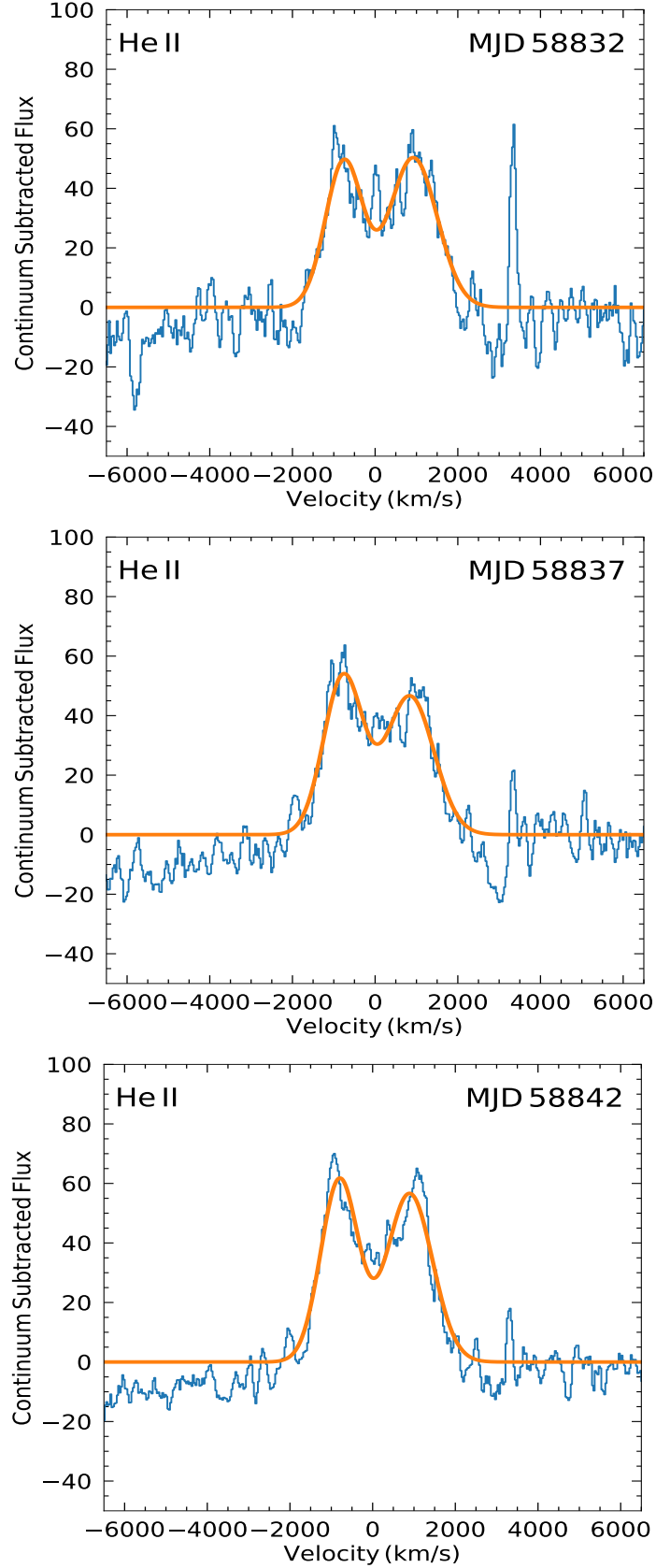
[12] https://github.com/trmrsh/trm-doppler

Figure 6. Best double-peak fit to the He II 4686 Å emission lines found in the Gemini/GMOS daily-averaged spectra of J0637. The *top*, *middle*, and *bottom* panels show data from MJD: 58832, 58837, and 58842, respectively. The best-fit (orange solid line) is overlaid on the data.

Table 1. Derived Emission Line Properties

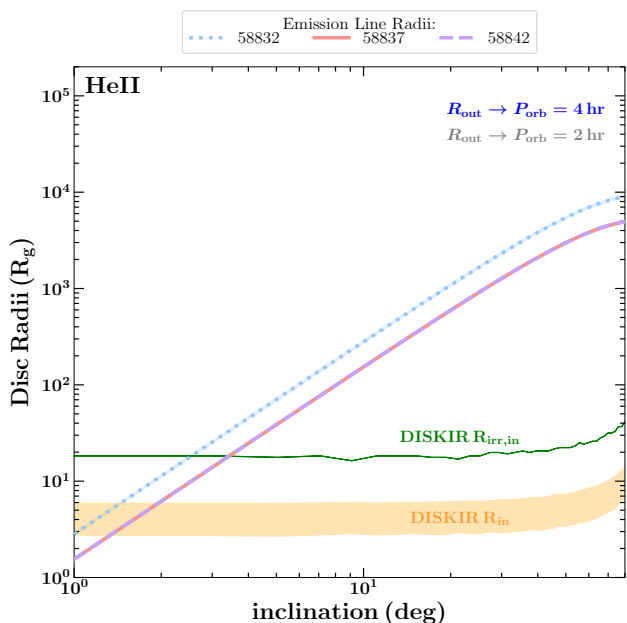| Time | Best Double-peak Fit | | | | | | FWHM | EW | DP | HWZI | v_{em} |
| | Peak 1 | | | Peak 2 | | | (km/s) | (Å) | (Å) | (Å) | (km/s) |
(MJD)	[μ_1	σ_1	A_1]	[μ_2	σ_2	A_2]					
					Emission Line: He II 4686 Å						
58832	4674.2(5)	7.1(1)	49(5)	4700.4(5)	9.0(1)	50(5)	2406(14)	−1972(202)	26.2(5)	31.9(5)	2041(31)
58837	4674.0(5)	7.4(1)	53(6)	4699.1(5)	9.1(1)	47(6)	2414(15)	−2064(241)	25.2(5)	43.1(6)	2759(39)
58842	4673.5(5)	7.1(1)	62(7)	4700.0(5)	8.6(1)	57(6)	2449(12)	−2306(260)	26.5(5)	43.0(5)	2752(35)

Figure 7. Radii within the disc at which the He II 4686 Å emission lines are emitted, as a function of binary inclination, for the three days in which Gemini/GMOS data was taken. Emission radii are compared to the inner disc radius ($R_{\rm in,DISKIR}$; orange shaded region) and inner radius of the optical/UV emitting portion of the disc ($R_{\rm irr,DISKIR}$; green shaded region) computed from the broad-band SED fits (see Section 4.1.2 and 4.3). Also plotted is the estimated outer disc radius, $R_{\rm out}$, corresponding to orbital periods of 2 (grey shaded region) and 4 hrs (dark blue shaded region). This analysis rules out low inclinations for this source.

use of both (i) estimates of $C_{\rm DISKIR}$, computed from the broad-band SED fits (see Section 4.1.2), as well as (ii) the C computed from a combination of bolometric and far-UV (UVM2, UVW2) light-curves (see Section 4.3), and (iii) $T_{\rm irr,DISKIR}$, computed from the broad-band SED fits (see Section 4.1.2). Unfortunately, $T_{\rm irr}$ is not well enough constrained using the light-curve method, largely due to our lack of knowledge of the orbital parameters of the system. Thus, we are not able to find a correlation with the emission line properties using this data.

Using the Spearman rank-order test[13] from the `scipy` package in PYTHON, we test for a positive correlation existing in each data-set. This algorithm calculates the Spearman correlation coefficient and its associated p-value. The correlation coefficent varies between -1 and 1, with a value of zero implying no correlation exists. The p-value represents the probability of an uncorrelated system producing the same correlation as the one computed from the data. To take into account uncertainties in the data, we perform monte-carlo sampling (1000 samples) over the the errors in each parameter, and take the mean of the sampled distribution as the final result.

For the FWHM vs. C correlation, the Spearman rank-order test results in (correlation coefficient, p-value) of (0.97,0.036), (1.0,0.0), and (1.0,0.0), for the FWHM correlation with $C_{\rm DISKIR,avg}$, $C_{\rm UVW2,lc}$, and $C_{\rm UVM2,lc}$, respectively. For the EW vs. C correlation, the Spearman rank-order test results in (correlation coefficient, p-value) of (0.99,0.015), (0.98,0.027), and (0.98,0.020), for the EW correlation with $C_{\rm DISKIR,avg}$, $C_{\rm UVW2,lc}$, and $C_{\rm UVM2,lc}$, respectively. For the FWHM vs. $T_{\rm irr,DISKIR}$, and EW vs. $T_{\rm irr,DISKIR}$, correlations, the Spearman rank-order test results in (correlation coefficient, p-value) of (1.0,0.0) and (0.98,0.027), respectively. Note that, for small data-sets like these ones, the stand-alone p-values are not particularly meaningful.

Changes in emission line profile shape (single-peaked vs double-peaked), as well emission line properties themselves (e.g., EW), during outburst have also been previously associated with spectral accretion state in BH-LMXBs (e.g., GROJ1655−40; Soria et al. 2000). Unfortunately, all of our Gemini/GMOS epochs were taken when J0637 was in the soft accretion state and no significant changes to properties of the X-ray spectrum irradiating the disc occurred during the 15-day time-period in which our Gemini/GMOS observations took place. While we cannot test for correlations between the He II 4686 Å emission line profile and spectral accretion state in our data, we do note that the double-peaked shape is a property that has been previously associated with soft-state BH-LMXBs (Soria et al. 2000).

These statistical results individually, combined with the fact

X-ray irradiation heating the disc in J0637 and the key properties of the H/He disc emission line profiles present in the Gemini/GMOS optical spectra. Below, we show our findings and use these correlations to demonstrate the connection between the line emitting regions of an LMXB disc and both the physical properties and spectrum of the X-ray irradiation heating said disc during outburst. Note that, as discussed earlier, the Hα region of our optical spectra is quite complex, here we focus our efforts on the strongest emission line found in our optical spectra, He II 4686 Å.

Using the line properties derived from our daily-averaged Gemini/GMOS spectra (see Section 4.4 and Table 1), we find evidence for positive correlations existing between (i) the fraction of X-rays intercepted and reprocessed in the outer disc (C) and both the FWHM and EW of the He II 4686 Å line, and (ii) the irradiation temperature in the outer disc region ($T_{\rm irr}$) and both the FWHM and EW of the He II 4686 Å line.

Figures 9 and 10 plots the correlations, found when making

---

[13] https://docs.scipy.org/doc/scipy/reference/generated/scipy.stats.spearmanr.html
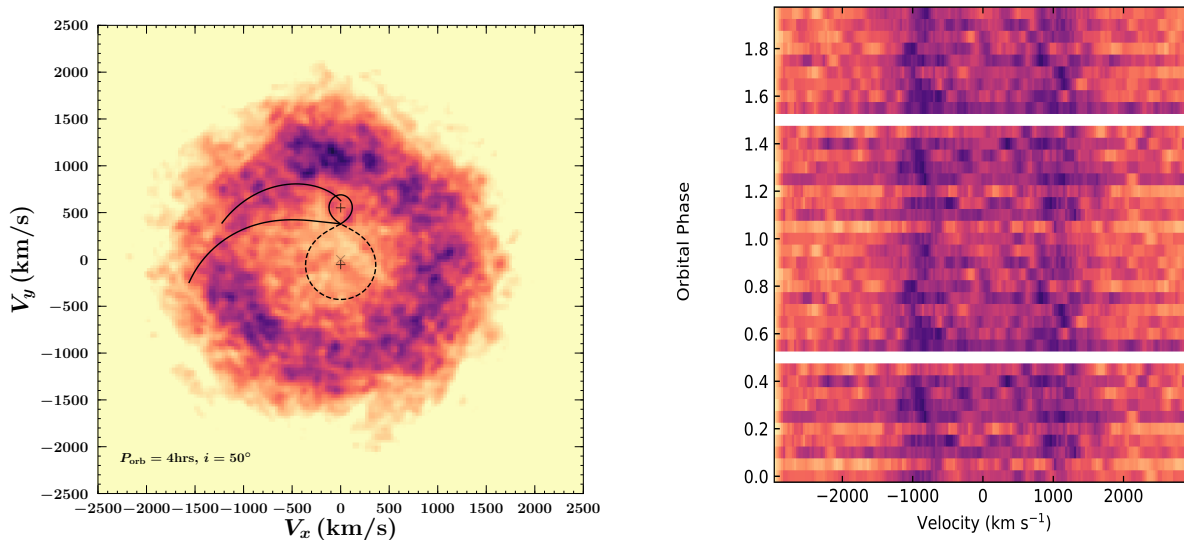
Figure 8. *(left)* Doppler tomogram of He II 4686 Å emission created from our full Gemini/GMOS data-set (7hrs on source). The tomogram is made assuming a P_{orb} = 4 hrs. The Roche lobes of the compact object (dashed black line) and companion star (solid black line) are displayed on the tomogram for an average over all binary inclination angles. *(right)* trailed spectrum, phase folded on a P_{orb} = 4 hrs.

that we observe statistical evidence for a positive correlation existing between the irradiation heating (C and T_{irr}) and both the FWHM and EW of the He II 4686 Å emission line, for irradiation properties computed using two completely independent methods (broad-band spectral fitting vs multi-wavelength time-series anlaysis), suggests that (i) the double-peaked emission line profiles in BH-LMXBs are likely the result of X-ray irradiation of the disc, and (ii) changes in physical properties of the irradiation-heating over an outburst can possibly be imprinted within the line profile properties themselves. Ultimately, more spectral data, taken over a larger range of time, flux, and spectral accretion state, during outburst, will allow us to put firmer constraints on the relationship between irradiation heating and disc emission line properties in BH-LMXBs.

6 SUMMARY

The double-peaked profiles of the H and He recombination lines observed in optical spectra can be used as powerful diagnostics for mapping the geometry and structure of the accretion discs in LMXB systems. In LMXBs, the detection of these emission lines during outburst is thought to be the result of X-ray irradiation heating the disc. This irradiation-heating plays a key role in regulating outburst cycles in these binary systems. By illuminating the disc surface, it controls both the overall evolution of an outburst from peak to quiescence, and the amount of mass able to be accreted during the outburst(Dubus et al. 1999, 2001a). However, despite decades of theoretical and observational efforts, the physical mechanism(s) driving X-ray irradiation remains largely unknown. The problem is three-fold. Neither (i) the disc radial profile, nor (ii) the geometry of the source heating such discs, nor (iii) the effect of the illuminating spectrum on the thermal properties of the disc, are well understood (Dubus et al. 1999, 2001a; Vrtilek et al. 1990; King et al. 1996). Answers to these open questions lie in understanding the evolution of the physical parameters of the irradiation source throughout an outburst cycle as functions of time and disc radius. These parameters

include: the fraction of the X-ray flux intercepted and reprocessed in the outer disc (C), the temperature at which the disc surface is heated (T_{irr}), and the spectrum of the irradiation source (Tetarenko et al. 2018a; Esin et al. 2000).

Accordingly, we have combined phase-resolved optical spectroscopy of new candidate BH-LMXB J0637, with multi-wavelength photometry, in an attempt to track and quantify how variations in irradiation-heating over an LMXB outburst affect the physical properties of the disc through its emission line profiles. We were able to monitor this system (on daily-weekly timescales) through its 8 month long outburst with *Swift*, obtaining time-series optical and UV photometry with UVOT, simultaneous with X-ray spectroscopic data from XRT. In addition, we were also able to obtain optical spectroscopic data from Gemini/GMOS during this time. These data are quasi-simultaneous over three individual days of the *Swift* monitoring, covering the end of the first viscous decay stage and transition to the irradiation-controlled decay stage in the light-curve.

Using the *Swift* UV, optical, and X-ray light-curves and spectra, we first derived the time-series evolution of key properties of the X-ray irradiation source heating the disc in J0637 over the entire outburst cycle using two independent observational methods. The first method involved fitting the broad-band (XRT+UVOT) SED with an irradiated disc model. The second method involved the recently developed empirical algorithm by Tetarenko et al. (2020), which makes use of multi-wavelength light-curves to build a three-dimensional X-ray irradiation profile (reprocessed fraction C, irradiation temperature T_{irr}, and size of the irradiated region of the disc R_{irr}) of the disc. Second, we fit double-peaked Gaussian profiles to the strongest emission line, He II 4686 Å, present in our daily-averaged Gemini/GMOS optical spectra. From here we were able to derive key properties defining these line profiles: FWHM, EW, DP seperation, and HWZI. Lastly, we built doppler tomograms, to analyze where in the disc the (irradiation-tracing) He II 4686 Å emission was coming from.
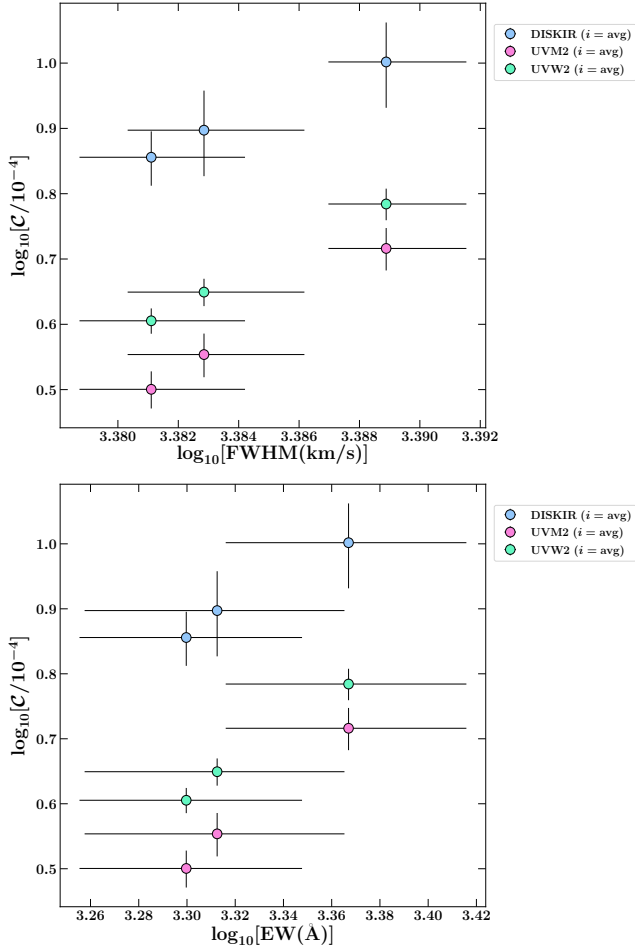
Figure 9. Correlation between the fraction of X-rays intercepted and reprocessed in the outer disc (C) and *(top)* FWHM (in km/s) and *(bottom)* EW (in Å) of the He II 4686 Å disc emission line. Positive correlations are plotted using X-ray irradiation heating computed from the (i) broad-band SED fits (DISKIR), assuming an average over all inclination angles (blue circles), and (ii) light-curve data in both the UVW2 (green circles) and UVM2 (pink circles) UVOT filters.

Figure 10. Correlation between the irradiation temperature in the outer disc region ($T_{\rm irr}$) and *(top)* FWHM (in km/s) and *(bottom)* EW (in Å) of the He II 4686 Å disc emission line. Positive correlations are plotted using X-ray irradiation heating computed from the broad-band SED fits (DISKIR), assuming an average over all inclination angles (blue circles).

Then, we looked for a correlation between the X-ray irradiation properties heating the disc in J0637 and the key parameters defining the detected He II 4686 Å emission line profiles. Making use of the Spearman rank-order test, we find statistical evidence for positive correlations existing between C and both the FWHM and EW of the He II 4686 Å line, and $T_{\rm irr}$ and both the FWHM and EW of the He II 4686 Å line. These positive correlations exist when making use of the X-ray irradiation properties derived from two independent observational methods, broad-band SED fitting and the light-curve comparision modelling of Tetarenko et al. (2020). These results provide both evidence for He recombination line profiles in LMXBs being caused by irradiation of the disc, and demonstrate that changes in physical properties of the irradiation-heating of the disc over an LMXB outburst can be imprinted within the He line profile themselves.

The pilot-program presented here is the first crucial step toward our overall goal of developing a method to use phase-resolved spectroscopy to effectively probe the geometry and structure of the gas making up an outbursting LMXB accretion disc. However, what

this pilot-study lacks is high-quality, sequential spectral data-sets, taken over a larger range of flux, and during different stages of the outburst decay, where the irradiating spectrum heating the disc changes significantly in shape. Future data will not only allow us to place firm constraints on the relationship we have found between irradiation-heating and disc emission line properties in LMXBs, but will also allow us to use multi-epoch tomography on higher time/wavelength resolution data, delivering a more coherent picture of accretion disc dynamics that one-off maps produced here do not (Marsh 2001, 2005).

ACKNOWLEDGEMENTS

DATA AVAILABILITY

The observational data presented in this work are available online in the HEASARC Archive (Swift ObsIds: 00012168001-00012172094; https://heasarc.gsfc.nasa.gov/docs/archive.html), Gemini Data Archive (Program ID: GS-2019B-Q-233, PI Tetarenko; https://archive.gemini.edu/), AAVSO International Database (https://www.aavso.org), and the Australia Telescope Online Archive (https://atoa.atnf.csiro.au/query.jsp).

REFERENCES

Arnaud K. A., 1996, in Jacoby G. H., Barnes J., eds, Astronomical Society of the Pacific Conference Series Vol. 101, Astronomical Data Analysis Software and Systems V. p. 17
Astropy Collaboration et al., 2013, A&A, 558, A33
Bernardini F., Russell D. M., Shaw A. W., Lewis F., Charles P. A., Koljonen K. I. I., Lasota J. P., Casares J., 2016, ApJ, 818, L5
Burrows D. N., et al., 2005, Space Sci. Rev., 120, 165
Casares J., 2015, ApJ, 808, 80
Casares J., 2016, ApJ, 822, 99
Charles P. A., Coe M. J., 2006, Optical, ultraviolet and infrared observations of X-ray binaries. pp 215–265
Coriat M., Fender R. P., Dubus G., 2012, MNRAS, 424, 1991
Crawford J. A., Kraft R. P., 1956, ApJ, 123, 44
Degenaar N., et al., 2014, ApJ, 784, 122
Dubus G., Lasota J.-P., Hameury J.-M., Charles P., 1999, MNRAS, 303, 139
Dubus G., Hameury J.-M., Lasota J.-P., 2001a, A&A, 373, 251
Dubus G., Kim R. S. J., Menou K., Szkody P., Bowen D. V., 2001b, ApJ, 553, 307
Esin A. A., Lasota J.-P., Hynes R. I., 2000, A&A, 354, 987
Event Horizon Telescope Collaboration et al., 2019, ApJ, 875, L1
Fitzpatrick E. L., Massa D., 1999, ApJ, 525, 1011

Frank J., King A., Raine D. J., 2002, Accretion Power in Astrophysics: Third Edition. Cambridge University Press
Gierliński M., Done C., Page K., 2009, MNRAS, 392, 1106
Güver T., Özel F., 2009, MNRAS, 400, 2050
Hambsch F. J., Myers G., Monard L. A. G., Patterson J., 2019, The Astronomer's Telegram, 13278, 1
Hameury J. M., 2020, Advances in Space Research, 66, 1004
Harrison F. A., et al., 2013, ApJ, 770, 103
Johar A., Russell D. M., Baglio M. C., Bramich D. M., Saikia P., Lewis F., 2020, The Astronomer's Telegram, 13779, 1
Kennea J. A., et al., 2019, The Astronomer's Telegram, 13257, 1
King A. R., Ritter H., 1998, MNRAS, 293, L42
King A. R., Kolb U., Burderi L., 1996, ApJ, 464, L127
Lomb N. R., 1976, Ap&SS, 39, 447
Marcel G., et al., 2019, A&A, 626, A115
Marsh T. R., 2001, Doppler Tomography. p. 1
Marsh T. R., 2005, Ap&SS, 296, 403
Marsh T. R., Horne K., 1988, MNRAS, 235, 269
Matsuoka M., et al., 2009, PASJ, 61, 999
McMullin J. P., Waters B., Schiebel D., Young W., Golap K., 2007, in Shaw R. A., Hill F., Bell D. J., eds, Astronomical Society of the Pacific Conference Series Vol. 376, Astronomical Data Analysis Software and Systems XVI. p. 127
Meshcheryakov A. V., Tsygankov S. S., Khamitov I. M., Shakura N. I., Bikmaev I. F., Eselevich M. V., Vlasyuk V. V., Pavlinsky M. N., 2018, MNRAS, 473, 3987
Migliari S., Fender R. P., 2006, MNRAS, 366, 79
Munari U., Zwitter T., 1997, A&A, 318, 269
Negoro H., et al., 2019, The Astronomer's Telegram, 13256, 1
Orosz J. A., Bailyn C. D., 1995, ApJ, 446, L59
Orosz J. A., Bailyn C. D., Remillard R. A., McClintock J. E., Foltz C. B., 1994, ApJ, 436, 848
Özel F., Psaltis D., Narayan R., McClintock J. E., 2010, ApJ, 725, 1918
Patterson J., et al., 2018, The Astronomer's Telegram, 11756, 1
Price-Whelan A. M., et al., 2018, AJ, 156, 123
Remillard R. A., McClintock J. E., 2006, ARA&A, 44, 49
Remillard R., Pasham D., Gendreau K., Arzoumanian Z., Homan J., Altamirano D., Steiner J., 2020, The Astronomer's Telegram, 13427, 1
Reynolds M. T., Miller J. M., 2013, ApJ, 769, 16
Roming P. W. A., et al., 2005, Space Sci. Rev., 120, 95
Russell T. D., et al., 2019a, ApJ, 883, 198
Russell T. D., Miller-Jones J. C. A., Sivakoff G. R., Tetarenko A. J., 2019b, The Astronomer's Telegram, 13275, 1
Rykoff E. S., Miller J. M., Steeghs D., Torres M. A. P., 2007, ApJ, 666, 1129
Scargle J. D., 1982, ApJ, 263, 835
Shaw A. W., Charles P. A., Casares J., Hernández Santisteban J. V., 2016, MNRAS, 463, 1314
Soria R., Wu K., Hunstead R. W., 2000, ApJ, 539, 445
Steeghs D., 2003, MNRAS, 344, 448
Steeghs D., 2004, Astronomische Nachrichten, 325, 185
Strader J., Aydi E., Sokolovsky K., Shishkovsky L., 2019, The Astronomer's Telegram, 13260, 1
Tetarenko B. E., Sivakoff G. R., Heinke C. O., Gladstone J. C., 2016, ApJS, 222, 15
Tetarenko B. E., Dubus G., Lasota J.-P., Heinke C. O., Sivakoff G. R., 2018a, MNRAS, 480, 2
Tetarenko B. E., Lasota J.-P., Heinke C. O., Dubus G., Sivakoff G. R., 2018b, Nature, 554, 69
Tetarenko B. E., Dubus G., Marcel G., Done C., Clavel M., 2020, MNRAS, 495, 3666
Tomsick J. A., Lazar H., 2020, The Astronomer's Telegram, 13800, 1
Tomsick J. A., et al., 2019, The Astronomer's Telegram, 13270, 1
Verner D. A., Ferland G. J., Korista K. T., Yakovlev D. G., 1996, ApJ, 465, 487
Vrtilek S. D., Raymond J. C., Garcia M. R., Verbunt F., Hasinger G., Kurster M., 1990, A&A, 235, 162
Wilms J., Allen A., McCray R., 2000, ApJ, 542, 914
Zechmeister M., Kürster M., 2009, A&A, 496, 577

Zurita C., Durant M., Torres M. A. P., Shahbaz T., Casares J., Steeghs D., 2008, ApJ, 681, 1458

van Dokkum P. G., 2001, PASP, 113, 1420

van Paradijs J., 1996, ApJ, 464, L139

van Paradijs J., McClintock J. E., 1994, A&A, 290, 133

APPENDIX A: GEMINI DATA DETAILS

Table A1: Gemini/GMOS Long-slit Data Details

Number	ObsID	Date	Time Start (UT)	Time End (UT)	Exposure Time (s)
1	20191215S0088	2019-12-15	05:15:42.2334	05:25:42.2334	600
2	20191215S0089	2019-12-15	05:26:34.1167	05:36:34.1167	600
3	20191215S0090	2019-12-15	05:37:26.4334	05:47:26.4334	600
4	20191215S0091	2019-12-15	05:48:19.4333	05:58:19.4334	600
5	20191215S0092	2019-12-15	05:59:11.3000	06:09:11.3000	600
6	20191215S0093	2019-12-15	06:10:03.1667	06:20:03.1667	600
7	20191215S0094	2019-12-15	06:20:54.2167	06:30:54.2167	600
8	20191215S0095	2019-12-15	06:31:46.2334	06:41:46.2334	600
9	20191215S0096	2019-12-15	06:42:39.3833	06:52:39.3834	600
10	20191215S0097	2019-12-15	06:53:30.2334	07:03:30.2334	600
11	20191215S0098	2019-12-15	07:04:22.1334	07:14:22.1334	600
12	20191220S0054	2019-12-20	04:09:12.3834	04:19:12.3834	600
13	20191220S0055	2019-12-20	04:20:03.1500	04:30:03.1500	600
14	20191220S0056	2019-12-20	04:30:54.1334	04:40:54.1334	600
15	20191220S0057	2019-12-20	04:41:45.1500	04:51:45.1500	600
16	20191220S0058	2019-12-20	04:52:36.1334	05:02:36.1334	600
17	20191220S0059	2019-12-20	05:03:28.4667	05:13:28.4667	600
18	20191220S0060	2019-12-20	05:14:20.1167	05:24:20.1167	600
19	20191220S0061	2019-12-20	05:25:11.834	05:35:11.834	600
20	20191220S0062	2019-12-20	05:36:02.834	05:46:02.834	600
21	20191220S0063	2019-12-20	05:46:53.4000	05:56:53.4000	600
22	20191220S0064	2019-12-20	05:57:45.1500	06:07:45.1500	600
23	20191225S0311	2019-12-25	03:30:53.8167	03:40:53.8167	600
24	20191225S0312	2019-12-25	03:41:44.9500	03:51:44.9500	600
25	20191225S0313	2019-12-25	03:52:36.8167	04:02:36.8167	600
26	20191225S0314	2019-12-25	04:03:28.9833	04:13:28.9834	600
27	20191225S0315	2019-12-25	04:14:20.9667	04:24:20.9667	600
28	20191225S0316	2019-12-25	04:25:12.8833	04:35:12.8834	600
29	20191225S0317	2019-12-25	04:36:04.8167	04:46:04.8167	600
30	20191225S0318	2019-12-25	04:46:57.1167	04:56:57.1167	600
31	20191225S0319	2019-12-25	04:57:48.9667	05:07:48.9667	600
32	20191225S0320	2019-12-25	05:08:40.9333	05:18:40.9334	600
33	20191225S0321	2019-12-25	05:19:32.9500	05:29:32.9500	600
34	20191225S0323	2019-12-25	05:31:52.9500	05:41:52.9500	600
35	20191225S0324	2019-12-25	05:42:44.9333	05:52:44.9334	600
36	20191225S0325	2019-12-25	05:53:34.9833	06:03:34.9834	600
37	20191225S0326	2019-12-25	06:04:28.9000	06:14:28.9000	600
38	20191225S0327	2019-12-25	06:15:21.834	06:25:21.834	600
39	20191225S0328	2019-12-25	06:26:11.9667	06:36:11.9667	600
40	20191225S0329	2019-12-25	06:37:04.8333	06:47:04.8334	600
41	20191225S0330	2019-12-25	06:47:56.9500	06:57:56.9500	600
42	20191225S0331	2019-12-25	06:58:48.9500	07:08:48.9500	600

APPENDIX B: DETAILED *SWIFT* SPECTRAL FIT DATA

Table B1: X-ray (XRT) Spectral Fits for MAXI J0637−430

ObsID[a]	MJD (days)	model fit[b]	F_X ($\times 10^{-10}$ erg cm^{-2} s^{-1})	T_{in} (keV)	γ	N_{pl} ($\times 10^{-4}$)	reduced χ^2_ν	dof
12168001a	58790.5828	0	$90.3^{+5.0}_{-4.8}$	$0.681^{+0.039}_{-0.037}$	$\cdots$	$\cdots$	0.98	110
12172001b	58794.0326	0	12.20 ± 0.13	0.6786 ± 0.0073	$\cdots$	$\cdots$	1.3	360
12172002	58795.9662	2	$85.44^{+0.77}_{-0.76}$	$0.782^{+0.012}_{-0.011}$	$1.76^{+0.13}_{-0.17}$	$2.10^{+0.61}_{-0.63}$	1.4	310
12172003	58796.7424	2	57.53 ± 0.34	$0.7337^{+0.0077}_{-0.0075}$	$1.959^{+0.058}_{-0.062}$	2.70 ± 0.33	1.3	380
12172004a	58797.8193	2	$65.39^{+0.40}_{-0.41}$	$0.7180^{+0.0078}_{-0.0076}$	$1.878^{+0.065}_{-0.073}$	$2.29^{+0.34}_{-0.33}$	1.1	370
12172004b	58797.8815	2	62.14 ± 0.40	$0.7211^{+0.0081}_{-0.0079}$	$1.959^{+0.073}_{-0.080}$	2.37 ± 0.36	1.1	390
12172005	58798.6026	0	$59.97^{+0.66}_{-0.65}$	$0.718^{+0.012}_{-0.011}$	$1.79^{+0.19}_{-0.33}$	$1.21^{+0.53}_{-0.58}$	1.2	290
12172006a	58799.6076	2	66.01 ± 0.38	$0.6713^{+0.0064}_{-0.0063}$	$2.139^{+0.071}_{-0.075}$	1.59 ± 0.21	1.2	370
12172006b	58799.6768	2	$58.56^{+0.34}_{-0.33}$	$0.6786^{+0.0065}_{-0.0063}$	$1.92^{+0.09}_{-0.10}$	1.33 ± 0.24	1.0	390
12172007a	58800.3939	0	73.0 ± 3.8	$0.623^{+0.040}_{-0.038}$	$\cdots$	$\cdots$	1.1	73
12172007b	58800.4601	2	65.72 ± 0.52	$0.6273^{+0.0090}_{-0.0087}$	$2.18^{+0.14}_{-0.16}$	1.00 ± 0.23	1.1	390
12172008a	58801.4022	2	39.93 ± 0.29	$0.6414^{+0.0078}_{-0.0075}$	$2.17^{+0.13}_{-0.15}$	$0.89^{+0.20}_{-0.21}$	1.2	310
12172008b	58801.9278	2	52.12 ± 0.26	$0.6664^{+0.0054}_{-0.0053}$	2.314 ± 0.073	1.22 ± 0.14	1.4	320
12172010a	58804.8447	2	41.20 ± 0.21	$0.6543^{+0.0061}_{-0.0060}$	$2.177^{+0.056}_{-0.058}$	$1.80^{+0.19}_{-0.18}$	1.2	400
12172010b	58804.9950	2	49.54 ± 0.39	$0.6376^{+0.0097}_{-0.0094}$	$2.12^{+0.09}_{-0.10}$	$1.71^{+0.30}_{-0.29}$	1.2	410
12172011	58805.9082	2	34.39 ± 0.25	$0.5791^{+0.0091}_{-0.0087}$	$2.116^{+0.051}_{-0.055}$	$2.30^{+0.31}_{-0.29}$	1.1	450
12172012	58806.3129	2	$31.75^{+0.32}_{-0.31}$	0.596 ± 0.012	$2.149^{+0.077}_{-0.082}$	$2.23^{+0.42}_{-0.38}$	1.1	370
12172013	58807.7646	2	44.49 ± 0.20	$0.6221^{+0.0052}_{-0.0051}$	$2.081^{+0.050}_{-0.053}$	1.63 ± 0.16	1.6	520
12172014	58808.8953	2	41.74 ± 0.18	$0.6175^{+0.0048}_{-0.0047}$	$2.196^{+0.060}_{-0.063}$	1.22 ± 0.13	1.3	490
12172015	58809.2947	2	41.35 ± 0.28	$0.5910^{+0.0073}_{-0.0070}$	2.27 ± 0.10	1.01 ± 0.17	1.3	400
12172016	58810.1059	0	35.32 ± 0.28	0.6284 ± 0.0047	$\cdots$	$\cdots$	1.3	280
12172018	58812.814	0	27.11 ± 0.13	0.5461 ± 0.0029	$\cdots$	$\cdots$	1.9	380
12172019	58813.2278	0	33.52 ± 0.24	0.5894 ± 0.0044	$\cdots$	$\cdots$	1.3	340
12172020	58814.1491	2	32.21 ± 0.19	$0.5768^{+0.0060}_{-0.0061}$	$2.73^{+0.18}_{-0.15}$	$0.616^{+0.099}_{-0.094}$	1.3	370
12172021a	58818.1966	0	$27.14^{+0.20}_{-0.19}$	0.5475 ± 0.0042	$\cdots$	$\cdots$	1.4	320
12172021b	58818.4035	2	36.29 ± 0.26	0.5281 ± 0.0063	$2.85^{+0.20}_{-0.17}$	$0.418^{+0.085}_{-0.081}$	1.4	320
12172021c	58818.2615	0	19.55 ± 0.14	0.5343 ± 0.0040	$\cdots$	$\cdots$	1.4	310
12172022a	58819.0045	2	27.30 ± 0.19	$0.5400^{+0.0062}_{-0.0063}$	$2.93^{+0.21}_{-0.17}$	$0.487^{+0.091}_{-0.086}$	1.2	330
12172022b	58819.0672	2	23.67 ± 0.14	$0.5422^{+0.0054}_{-0.0055}$	$2.92^{+0.16}_{-0.13}$	$0.573^{+0.081}_{-0.078}$	1.5	350
12172023	58820.8515	2	25.88 ± 0.12	0.5364 ± 0.0043	$2.850^{+0.109}_{-0.097}$	$0.559^{+0.061}_{-0.059}$	1.4	390
12172024	58821.1917	2	24.39 ± 0.15	0.5112 ± 0.0058	$2.75^{+0.14}_{-0.13}$	$0.460^{+0.074}_{-0.071}$	1.1	330
12172025	58822.6442	2	22.78 ± 0.18	$0.5215^{+0.0073}_{-0.0074}$	$2.85^{+0.22}_{-0.18}$	$0.467^{+0.096}_{-0.090}$	1.1	300
12172026	58823.9753	2	18.76 ± 0.10	0.5236 ± 0.0050	$0.8^{+2.1}_{-1.9}$	$0.583^{+0.071}_{-0.068}$	1.4	360
12172027	58824.8343	2	22.36 ± 0.11	0.4955 ± 0.0044	$2.729^{+0.077}_{-0.076}$	$0.523^{+0.059}_{-0.057}$	1.4	370
12172028	58825.9005	2	21.83 ± 0.16	0.5128 ± 0.0064	$2.81^{+0.16}_{-0.15}$	$0.457^{+0.083}_{-0.079}$	1.1	320
12172029	58826.6273	2	21.68 ± 0.11	$0.5046^{+0.4955}_{-0.0042}$	$2.861^{+0.092}_{-0.087}$	$0.474^{+0.055}_{-0.053}$	1.4	360
12172030	58827.0259	2	20.82 ± 0.11	0.5079 ± 0.0046	$2.849^{+0.098}_{-0.092}$	$0.516^{+0.060}_{-0.058}$	1.4	360
12172031	58828.6267	2	18.52 ± 0.21	0.503 ± 0.010	$2.92^{+0.31}_{-0.24}$	$0.43^{+0.12}_{-0.11}$	1.2	260
12172032	58829.5478	2	19.21 ± 0.12	$0.4831^{+0.0055}_{-0.0054}$	$2.81^{+0.12}_{-0.11}$	$0.413^{+0.064}_{-0.062}$	1.1	320
12172033a	58830.6098	2	17.06 ± 0.12	0.4726 ± 0.0058	$3.07^{+0.14}_{-0.13}$	$0.403^{+0.062}_{-0.058}$	1.3	300
12172033b	58830.6859	2	18.82 ± 0.15	0.4734 ± 0.0067	$2.95^{+0.14}_{-0.13}$	$0.421^{+0.075}_{-0.070}$	1.3	280
12172034a	58831.5451	2	17.87 ± 0.12	0.4728 ± 0.0054	$3.10^{+0.11}_{-0.10}$	$0.470^{+0.061}_{-0.058}$	1.3	310
12172034b	58831.6057	2	18.60 ± 0.13	$0.4711^{+0.0058}_{-0.0057}$	$2.88^{+0.11}_{-0.10}$	$0.436^{+0.066}_{-0.063}$	1.2	310
12172035a	58832.5348	2	16.96 ± 0.11	$0.4626^{+0.0055}_{-0.0054}$	2.94 ± 0.11	$0.376^{+0.058}_{-0.055}$	1.2	300
12172035b	58832.6011	2	17.64 ± 0.11	$0.4704^{+0.0056}_{-0.0055}$	2.86 ± 0.11	$0.413^{+0.061}_{-0.059}$	1.2	310
12172036	58833.8724	2	$16.839^{+0.096}_{-0.095}$	0.4733 ± 0.0046	$3.12^{+0.12}_{-0.11}$	$0.372^{+0.048}_{-0.046}$	1.2	320
12172037	58834.599	2	16.26 ± 0.11	0.4668 ± 0.0057	$3.14^{+0.14}_{-0.12}$	$0.395^{+0.061}_{-0.057}$	1.1	300
12172038a	58835.5906	2	$16.34^{+0.13}_{-0.12}$	$0.4639^{+0.0064}_{-0.0063}$	$2.93^{+0.13}_{-0.12}$	$0.416^{+0.069}_{-0.065}$	1.2	290

Table B1: X-ray (XRT) Spectral Fits for MAXI J0637−430

ObsID[a]	MJD (days)	model fit[b]	F_X ($\times 10^{-10}$ erg cm^{-2} s^{-1})	T_{in} (keV)	γ	N_{pl} ($\times 10^{-4}$)	reduced χ^2_ν	dof
12172038b	58835.6554	2	17.13 ± 0.14	$0.4821^{+0.0071}_{-0.0072}$	$3.04^{+0.21}_{-0.17}$	$0.410^{+0.078}_{-0.073}$	1.0	280
12172039	58836.7168	2	14.909 ± 0.087	0.4452 ± 0.0047	$2.944^{+0.085}_{-0.084}$	$0.369^{+0.047}_{-0.045}$	1.4	320
12172040	58837.6459	2	14.920 ± 0.080	0.4458 ± 0.0043	$2.910^{+0.080}_{-0.079}$	$0.367^{+0.044}_{-0.042}$	1.4	330
12172041	58839.6383	2	13.53 ± 0.15	$0.4282^{+0.0091}_{-0.0089}$	$3.03^{+0.17}_{-0.16}$	$0.345^{+0.084}_{-0.076}$	1.2	230
12172042	58840.6992	2	13.305 ± 0.081	$0.4305^{+0.0051}_{-0.0050}$	2.920 ± 0.076	$0.414^{+0.052}_{-0.049}$	1.4	310
12172043a	58841.6469	2	13.04 ± 0.12	$0.4340^{+0.0075}_{-0.0074}$	$2.98^{+0.20}_{-0.19}$	$0.269^{+0.062}_{-0.058}$	1.1	250
12172043b	58841.7734	2	11.147 ± 0.088	$0.4286^{+0.0063}_{-0.0062}$	$3.02^{+0.12}_{-0.11}$	$0.334^{+0.057}_{-0.053}$	1.6	270
12172044a	58842.6917	2	12.56 ± 0.10	$0.4166^{+0.0063}_{-0.0060}$	$2.81^{+0.13}_{-0.14}$	$0.266^{+0.056}_{-0.053}$	1.3	270
12172044b	58842.7578	2	12.59 ± 0.11	$0.4218^{+0.0071}_{-0.0069}$	$2.88^{+0.14}_{-0.15}$	$0.282^{+0.062}_{-0.058}$	1.2	260
12172045a	58843.699	2	17.72 ± 0.14	$0.4123^{+0.0066}_{-0.0064}$	2.994 ± 0.093	$0.376^{+0.062}_{-0.057}$	1.4	270
12172045b	58843.7645	2	13.77 ± 0.14	$0.4148^{+0.0085}_{-0.0082}$	2.98 ± 0.12	$0.377^{+0.081}_{-0.073}$	1.2	240
12172046a	58844.289	2	11.58 ± 0.10	$0.4307^{+0.0073}_{-0.0071}$	2.90 ± 0.12	$0.366^{+0.072}_{-0.067}$	1.2	260
12172046b	58844.3522	2	12.16 ± 0.11	$0.4319^{+0.0071}_{-0.0069}$	$2.80^{+0.14}_{-0.15}$	$0.304^{+0.068}_{-0.065}$	1.1	260
12172047	58845.8187	2	11.422 ± 0.090	$0.4031^{+0.0063}_{-0.0061}$	$2.977^{+0.093}_{-0.094}$	$0.337^{+0.056}_{-0.052}$	1.1	270
12172048a	58846.8847	2	11.13 ± 0.10	$0.4050^{+0.0070}_{-0.0067}$	$2.83^{+0.15}_{-0.16}$	$0.232^{+0.057}_{-0.054}$	1.3	240
12172048b	58846.9539	2	10.34 ± 0.23	$0.401^{+0.018}_{-0.016}$	$2.94^{+0.28}_{-0.30}$	$0.32^{+0.17}_{-0.14}$	0.94	160
12172049a	58847.7398	2	$11.30^{+0.11}_{-0.12}$	$0.3915^{+0.0050}_{-0.0041}$	$2.06^{+0.26}_{-0.27}$	$0.054^{+0.029}_{-0.020}$	1.6	250
12172049b	58847.8106	2	$10.682^{+0.097}_{-0.095}$	0.3984 ± 0.0035	$1.80^{+0.25}_{-0.40}$	$0.040^{+0.021}_{-0.019}$	1.5	270
12172050	58848.883	2	9.72 ± 0.19	$0.398^{+0.015}_{-0.013}$	$2.88^{+0.27}_{-0.32}$	$0.26^{+0.13}_{-0.11}$	0.97	170
12172051a	58849.7313	2	10.466 ± 0.089	$0.3912^{+0.0062}_{-0.0059}$	$2.86^{+0.11}_{-0.12}$	$0.246^{+0.051}_{-0.047}$	1.3	260
12172051b	58849.8012	2	10.114 ± 0.093	$0.3882^{+0.0067}_{-0.0064}$	$2.87^{+0.13}_{-0.14}$	$0.221^{+0.051}_{-0.047}$	1.2	240
12172052	58850.2593	2	9.986 ± 0.090	$0.4058^{+0.0067}_{-0.0064}$	$2.85^{+0.15}_{-0.16}$	$0.222^{+0.054}_{-0.051}$	1.3	250
12172053	58851.254	2	10.149 ± 0.091	$0.3926^{+0.0064}_{-0.0062}$	$3.09^{+0.14}_{-0.13}$	$0.218^{+0.045}_{-0.042}$	1.3	240
12172054	58852.4495	2	9.672 ± 0.089	$0.3886^{+0.0065}_{-0.0063}$	$2.99^{+0.15}_{-0.16}$	$0.191^{+0.046}_{-0.043}$	1.1	240
12172055	58853.3848	2	8.99 ± 0.11	$0.3779^{+0.0081}_{-0.0075}$	$2.86^{+0.18}_{-0.21}$	$0.175^{+0.057}_{-0.053}$	1.1	220
12172056	58854.315	2	8.987 ± 0.068	$0.3736^{+0.0053}_{-0.0050}$	$2.90^{+0.10}_{-0.11}$	$0.192^{+0.037}_{-0.034}$	1.4	260
12172057	58855.643	2	$9.166^{+0.081}_{-0.082}$	$0.3967^{+0.0071}_{-0.0069}$	3.07 ± 0.11	$0.329^{+0.059}_{-0.054}$	1.2	250
12172059a	58857.0981	2	8.310 ± 0.084	$0.3535^{+0.0070}_{-0.0065}$	$2.88^{+0.13}_{-0.15}$	$0.175^{+0.046}_{-0.041}$	1.4	220
12172059b	58857.1742	2	8.761 ± 0.088	$0.3755^{+0.0071}_{-0.0067}$	$2.87^{+0.13}_{-0.15}$	$0.208^{+0.053}_{-0.048}$	1.2	230
12172060a	58858.426	2	8.868 ± 0.089	$0.3513^{+0.0066}_{-0.0060}$	$2.56^{+0.10}_{-0.12}$	$0.238^{+0.060}_{-0.051}$	1.2	250
12172060b	58858.4916	2	9.32 ± 0.10	$0.3714^{+0.0085}_{-0.0078}$	$2.66^{+0.11}_{-0.13}$	$0.308^{+0.083}_{-0.071}$	1.3	240
12172064	58864.6897	2	3.30 ± 0.15	0.174 ± 0.014	2.01 ± 0.20	$0.0182^{+0.0070}_{-0.0050}$	1.1	120
12172066	58866.6131	2	$2.901^{+0.098}_{-0.096}$	$0.1648^{+0.0097}_{-0.0096}$	1.95 ± 0.13	$0.0133^{+0.0037}_{-0.0029}$	1.0	160
12172067a	58869.4598	2	$1.505^{+0.096}_{-0.093}$	$0.124^{+0.016}_{-0.015}$	1.71 ± 0.13	$0.0046^{+0.0044}_{-0.0024}$	0.78	97
12172067b	58869.2	2	$1.370^{+0.063}_{-0.061}$	$0.132^{+0.014}_{-0.013}$	1.81 ± 0.11	$0.0067^{+0.0043}_{-0.0028}$	0.95	150
12172071	58873.9762	1	0.703 ± 0.030	$\cdots$	$2.066^{+0.065}_{-0.063}$	$\cdots$	1.1	280
12172072	58874.5156	1	$0.606^{+0.047}_{-0.046}$	$\cdots$	$2.02^{+0.12}_{-0.11}$	$\cdots$	1.0	160
12172073	58875.4391	1	$0.642^{+0.040}_{-0.039}$	$\cdots$	$1.929^{+0.085}_{-0.082}$	$\cdots$	1.0	210
12172074	58876.5592	1	$0.480^{+0.036}_{-0.035}$	$\cdots$	$1.804^{+0.098}_{-0.095}$	$\cdots$	0.95	190
12172075	58877.0235	1	$0.485^{+0.039}_{-0.038}$	$\cdots$	$1.93^{+0.11}_{-0.10}$	$\cdots$	0.86	140
12172076	58878.1523	1	$0.402^{+0.040}_{-0.038}$	$\cdots$	1.74 ± 0.12	$\cdots$	0.91	140
12172077	58879.2234	1	$0.380^{+0.028}_{-0.027}$	$\cdots$	$1.689^{+0.090}_{-0.088}$	$\cdots$	1.1	200
12172080	58885.7255	1	$0.228^{+0.032}_{-0.033}$	$\cdots$	$1.51^{+0.20}_{-0.13}$	$\cdots$	0.80	60
12172081	58886.1173	1	$0.263^{+0.086}_{-0.064}$	$\cdots$	$1.38^{+0.45}_{-0.15}$	$\cdots$	0.58	20
12172082	58887.1160	1	$0.190^{+0.031}_{-0.022}$	$\cdots$	$1.62^{+0.29}_{-0.12}$	$\cdots$	0.81	46
12172083	58888.8541	1	$0.216^{+0.028}_{-0.025}$	$\cdots$	$1.46^{+0.25}_{-0.11}$	$\cdots$	0.73	50
12172084	58889.5696	1	$0.180^{+0.063}_{-0.039}$	$\cdots$	$1.94^{+0.76}_{-0.54}$	$\cdots$	1.0	23
12172085	58890.4982	1	$0.227^{+0.035}_{-0.032}$	$\cdots$	$1.51^{+0.30}_{-0.13}$	$\cdots$	0.69	46
12172086	58891.1628	1	$0.093^{+0.017}_{-0.014}$	$\cdots$	$1.44^{+0.25}_{-0.14}$	$\cdots$	0.88	44

Table B1: X-ray (XRT) Spectral Fits for MAXI J0637−430

ObsID[a]	MJD (days)	model fit[b]	F_X ($\times 10^{-10}$ erg cm^{-2} s^{-1})	T_{in} (keV)	γ	N_{pl} ($\times 10^{-4}$)	reduced χ^2_ν	dof
12172087	58892.2259	1	$0.168^{+0.024}_{-0.022}$	$\cdots$	$1.49^{+0.29}_{-0.18}$	$\cdots$	0.97	65
12172088	58893.1549	1	$0.127^{+0.016}_{-0.015}$	$\cdots$	$1.66^{+0.30}_{-0.15}$	$\cdots$	0.82	71
12172089	58894.2224	1	0.153 ± 0.016	$\cdots$	$1.64^{+0.23}_{-0.22}$	$\cdots$	0.77	90
12172090	58896.1467	1	$0.150^{+0.023}_{-0.022}$	$\cdots$	$1.64^{+0.34}_{-0.19}$	$\cdots$	0.76	52
12172091	58902.8604	1	$0.103^{+0.020}_{-0.017}$	$\cdots$	$1.61^{+0.27}_{-0.18}$	$\cdots$	0.82	41
12172092	58909.8978	1	$0.086^{+0.046}_{-0.020}$	$\cdots$	$2.49^{+0.76}_{-0.59}$	$\cdots$	0.85	28
12172093	58916.871	1	$0.083^{+0.042}_{-0.031}$	$\cdots$	$1.36^{+0.52}_{-0.49}$	$\cdots$	0.52	7.0
12172094	58923.9088	1	$0.044^{+0.011}_{-0.010}$	$\cdots$	$1.85^{+0.35}_{-0.32}$	$\cdots$	0.59	16

[a]ObsIDs containing letters are observations that have been split into multiple GTIs.

[b] `tbabs*cflux*diskbb` (model 0), `tbabs*cflux*powerlaw` (model 1), `tbabs*cflux*(diskbb+powerlaw)` (model 2).

Note: for use of the `cflux` xspec model component to obtain a flux estimate, either the `diskbb` normalization (for models 0 and 2) or `powerlaw` normalization (for model 1) must be frozen at 1.0.

Table B2: Broad-band (XRT+UVOT) Spectral Fits for MAXI J0637−430

ObsID[a]	MJD (days)	T_{in} (keV)	f_{out}	logrout	N_{disc}	L_c/L_d[b]	reduced χ^2	dof
12172001	58794.0326	$0.71166^{+0.00585}_{-0.00599}$	$377.9^{+34.9}_{-35.4}$	$4.5428^{+0.0248}_{-0.0211}$	$233.72^{+8.94}_{-8.19}$	0.0	1.81	364
12172002	58795.9662	0.7667 ± 0.0143	$24.46^{+4.16}_{-3.22}$	$4.1689^{+0.0455}_{-0.0467}$	$1144.2^{+69.4}_{-64.1}$	$0.3820^{+0.0710}_{-0.0690}$	1.44	319
12172003	58796.7424	$0.70719^{+0.00911}_{-0.00913}$	$79.3^{+13.2}_{-10.6}$	4.0988 ± 0.0297	$1034.2^{+44.6}_{-42.4}$	$0.4641^{+0.0464}_{-0.0454}$	1.34	384
12172004a	58797.8193	$0.69294^{+0.00943}_{-0.00944}$	$65.65^{+10.23}_{-8.33}$	$4.0330^{+0.0281}_{-0.0282}$	$1268.8^{+57.2}_{-54.0}$	$0.5015^{+0.0490}_{-0.0481}$	1.09	371
12172004b	58797.8815	0.6807 ± 0.0105	$71.99^{+11.94}_{-9.54}$	$4.0230^{+0.0291}_{-0.0294}$	$1286.6^{+66.4}_{-62.2}$	$0.4319^{+0.0499}_{-0.0489}$	1.14	393
12172005	58798.6026	$0.7084^{+0.0165}_{-0.0162}$	$81.8^{+35.2}_{-22.0}$	$4.0379^{+0.0523}_{-0.0517}$	$1106.2^{+86.7}_{-82.5}$	$0.3242^{+0.0781}_{-0.0765}$	1.26	242
12172006a	58799.6076	$0.69404^{+0.00577}_{-0.00573}$	$65.14^{+8.93}_{-7.45}$	$4.0288^{+0.0263}_{-0.0264}$	$1475.6^{+42.7}_{-41.5}$	0.1	1.41	323
12172006b	58799.6076	$0.66826^{+0.00770}_{-0.00769}$	$72.43^{+10.72}_{-8.73}$	$4.0326^{+0.0275}_{-0.0278}$	$1379.2^{+53.8}_{-51.4}$	$0.3493^{+0.0403}_{-0.0398}$	1.02	378
12172007a	58800.3939	$0.6378^{+0.0419}_{-0.0394}$	$85.3^{+31.2}_{-19.4}$	$3.8392^{+0.0741}_{-0.0759}$	$2371^{+681.4}_{-529}$	0.1	1.14	76.0
12172007b	58800.4601	$0.64098^{+0.00486}_{-0.00481}$	$93.3^{+27.4}_{-18.8}$	$3.8899^{+0.0465}_{-0.0471}$	$2002.4^{+64.7}_{-64.2}$	$0.2044^{+0.0460}_{-0.0456}$	1.12	394
12172008a	58801.4022	$0.64959^{+0.00528}_{-0.00530}$	$129.0^{+19.2}_{-15.6}$	$4.0559^{+0.0261}_{-0.0264}$	$1122.8^{+35.6}_{-34.5}$	0.1	1.24	251
12172008b	58801.9278	0.67458 ± 0.00320	$94.4^{+13.5}_{-11.0}$	$4.0294^{+0.0254}_{-0.0258}$	$1287.8^{+23.9}_{-23.8}$	0.1	1.38	331
12172009	58803.7124	$0.63314^{+0.00716}_{-0.00717}$	$41.35^{+7.08}_{-5.57}$	$3.8671^{+0.0312}_{-0.0319}$	$2649.5^{+100.7}_{-95.8}$	$0.4099^{+0.0350}_{-0.0345}$	1.23	355
12172010a	58804.8447	$0.61965^{+0.00762}_{-0.00765}$	$90.3^{+14.6}_{-11.6}$	$4.0170^{+0.0292}_{-0.0297}$	$1299.5^{+55.4}_{-52.5}$	$0.4035^{+0.0369}_{-0.0364}$	1.01	335
12172010b	58804.9950	$0.61693^{+0.00908}_{-0.00901}$	$71.58^{+11.66}_{-9.25}$	$3.9731^{+0.0301}_{-0.0308}$	$1623.4^{+84.4}_{-79.8}$	$0.4009^{+0.0546}_{-0.0537}$	1.21	416
12172011	58805.9082	$0.52217^{+0.00777}_{-0.00772}$	$68.66^{+10.99}_{-8.61}$	$3.9478^{+0.0324}_{-0.0333}$	$1971.6^{+105.8}_{-99.9}$	$0.8793^{+0.0634}_{-0.0622}$	1.11	448
12172012	58806.3129	$0.5517^{+0.0110}_{-0.0109}$	$109.1^{+24.3}_{-17.7}$	$3.9575^{+0.0368}_{-0.0375}$	$1497^{+110.1}_{-103}$	$0.6917^{+0.0764}_{-0.0744}$	1.09	374
12172013	58807.7646	$0.59949^{+0.00499}_{-0.00495}$	$67.67^{+10.79}_{-8.59}$	$3.9775^{+0.0305}_{-0.0310}$	$1617.4^{+48.1}_{-47.0}$	$0.4559^{+0.0302}_{-0.0300}$	1.61	525
12172014	58808.8953	$0.60779^{+0.00452}_{-0.00449}$	$73.77^{+12.09}_{-9.61}$	$3.9671^{+0.0310}_{-0.0314}$	$1519.1^{+41.1}_{-40.2}$	$0.2808^{+0.0249}_{-0.0247}$	1.31	494
12172015	58809.2947	$0.58267^{+0.00654}_{-0.00648}$	$66.79^{+11.55}_{-8.98}$	$3.9212^{+0.0338}_{-0.0348}$	$1824.5^{+74.6}_{-71.6}$	$0.2525^{+0.0362}_{-0.0359}$	1.31	407
12172016	58810.1059	0.6168 ± 0.0110	$121.3^{+33.0}_{-23.7}$	$3.9481^{+0.0443}_{-0.0437}$	$1239.5^{+78.8}_{-73.3}$	$0.1357^{+0.0470}_{-0.0463}$	1.05	212
12172018	58812.814	$0.55017^{+0.00296}_{-0.00295}$	$131.5^{+26.3}_{-20.0}$	$3.8824^{+0.0331}_{-0.0336}$	$1627.2^{+39.8}_{-39.7}$	0.1	1.32	381
12172019	58813.2278	$0.59218^{+0.00445}_{-0.00443}$	$80.4^{+20.5}_{-14.5}$	$3.9621^{+0.0505}_{-0.0516}$	$1482.3^{+47.4}_{-46.2}$	0.1	1.31	343
12172020	58814.1491	$0.57378^{+0.00342}_{-0.00340}$	$107.5^{+24.5}_{-18.1}$	$3.8993^{+0.0395}_{-0.0401}$	$1594.0^{+41.9}_{-41.5}$	0.1	1.26	378
12172021a	58818.1966	$0.55016^{+0.00419}_{-0.00416}$	$102.1^{+19.2}_{-14.7}$	$3.8674^{+0.0335}_{-0.0343}$	$1639.7^{+53.8}_{-52.3}$	0.1	1.38	320
12172021b	58818.4035	$0.52378^{+0.00379}_{-0.00377}$	$76.5^{+15.7}_{-11.7}$	$3.7525^{+0.0353}_{-0.0367}$	$2690.3^{+84.1}_{-81.7}$	0.1	1.34	325
12172021c	58818.2615	$0.55356^{+0.00413}_{-0.00412}$	$162.5^{+31.9}_{-24.1}$	$3.9342^{+0.0335}_{-0.0342}$	$1167.9^{+38.8}_{-37.9}$	0.0	1.18	317
12172022a	58819.0045	$0.53266^{+0.00383}_{-0.00381}$	$85.6^{+14.8}_{-11.4}$	$3.8642^{+0.0334}_{-0.0345}$	$1875.2^{+57.9}_{-56.3}$	0.1	1.17	333
12172022b	58819.0672	$0.53396^{+0.00323}_{-0.00322}$	$102.1^{+18.1}_{-13.8}$	$3.8949^{+0.0332}_{-0.0345}$	$1598.4^{+42.1}_{-41.3}$	0.1	1.46	352
12172023	58820.8515	$0.53043^{+0.00249}_{-0.00248}$	$94.0^{+19.7}_{-14.4}$	$3.8490^{+0.0374}_{-0.0391}$	$1801.5^{+37.6}_{-37.5}$	0.1	1.40	392
12172024	58821.1917	$0.50991^{+0.00471}_{-0.00467}$	$89.1^{+16.2}_{-12.3}$	$3.8558^{+0.0355}_{-0.0367}$	$2015.5^{+72.9}_{-70.5}$	0.1	1.10	340
12172025	58822.6442	$0.51740^{+0.00420}_{-0.00417}$	$111.9^{+39.6}_{-26.0}$	$3.8450^{+0.0511}_{-0.0516}$	$1760.3^{+64.8}_{-64.2}$	0.1	1.04	305
12172026	58823.9753	$0.51808^{+0.00292}_{-0.00291}$	$106.5^{+19.9}_{-14.8}$	$3.9301^{+0.0372}_{-0.0390}$	$1438.0^{+35.8}_{-35.3}$	0.1	1.40	365
12172027	58824.8343	$0.48960^{+0.00345}_{-0.00343}$	$63.19^{+12.38}_{-8.96}$	$3.8806^{+0.0488}_{-0.0527}$	$2186.7^{+60.9}_{-59.4}$	0.1	1.37	372
12172028	58825.9005	$0.51036^{+0.00374}_{-0.00372}$	$122.6^{+36.5}_{-24.8}$	$3.7904^{+0.0454}_{-0.0466}$	$1783.7^{+59.6}_{-59.2}$	0.1	1.12	321
12172029	58826.6273	$0.49987^{+0.00254}_{-0.00253}$	$90.2^{+17.6}_{-13.1}$	$3.8473^{+0.0381}_{-0.0398}$	$1953.9^{+44.2}_{-43.5}$	0.1	1.34	365
12172030	58827.0259	$0.50336^{+0.00268}_{-0.00267}$	$111.5^{+26.9}_{-19.0}$	$3.8123^{+0.0406}_{-0.0426}$	$1807.7^{+44.2}_{-44.1}$	0.1	1.32	365
12172031	58828.6267	$0.49698^{+0.00560}_{-0.00558}$	$78.9^{+24.0}_{-15.4}$	$3.9203^{+0.0663}_{-0.0705}$	$1720.5^{+85.4}_{-81.2}$	0.1	1.12	262
12172032	58829.5478	$0.48073^{+0.00431}_{-0.00427}$	$103.0^{+27.3}_{-18.6}$	$3.7876^{+0.0462}_{-0.0487}$	$2039.5^{+74.8}_{-72.8}$	0.1	1.04	326
12172033a	58830.6098	$0.46345^{+0.00340}_{-0.00337}$	$117.0^{+26.0}_{-18.6}$	$3.7613^{+0.0382}_{-0.0401}$	$2126.5^{+70.6}_{-68.8}$	0.1	1.26	303
12172033b	58830.6859	$0.46735^{+0.00391}_{-0.00390}$	$103.7^{+22.3}_{-16.2}$	$3.7516^{+0.0380}_{-0.0398}$	$2265.5^{+85.1}_{-82.1}$	0.1	1.30	291
12172034a	58831.5451	$0.46035^{+0.00317}_{-0.00316}$	$91.4^{+16.6}_{-12.4}$	$3.7936^{+0.0362}_{-0.0380}$	$2302.8^{+70.9}_{-68.8}$	0.1	1.38	314
12172034b	58831.6057	$0.46701^{+0.00331}_{-0.00330}$	$86.1^{+14.8}_{-11.4}$	$3.8038^{+0.0356}_{-0.0369}$	$2252.8^{+70.9}_{-68.6}$	0.1	1.15	312
12172035a	58832.5348	$0.45805^{+0.00323}_{-0.00322}$	$99.3^{+19.6}_{-14.5}$	$3.7752^{+0.0376}_{-0.0392}$	$2234.3^{+71.0}_{-68.8}$	0.1	1.23	308
12172035b	58832.6011	$0.46761^{+0.00314}_{-0.00313}$	$96.1^{+18.9}_{-14.0}$	$3.7869^{+0.0374}_{-0.0391}$	$2120.5^{+63.8}_{-62.1}$	0.1	1.21	317
12172036	58833.8724	$0.46329^{+0.00276}_{-0.00274}$	$96.6^{+25.3}_{-17.2}$	$3.7535^{+0.0462}_{-0.0490}$	$2117.1^{+57.5}_{-56.7}$	0.1	1.31	327
12172037	58834.599	$0.45508^{+0.00337}_{-0.00336}$	$76.8^{+19.4}_{-13.2}$	$3.7939^{+0.0520}_{-0.0556}$	$2219.4^{+73.8}_{-71.5}$	0.1	1.20	302
12172038a	58835.5906	0.45863 ± 0.00360	$84.4^{+15.9}_{-11.9}$	$3.7985^{+0.0394}_{-0.0412}$	$2144.9^{+75.3}_{-72.6}$	0.1	1.22	292

Table B2: Broad-band (XRT+UVOT) Spectral Fits for MAXI J0637−430

ObsID[a]	MJD (days)	T_{in} (keV)	f_{out}	logrout	N_{disc}	L_c/L_d[b]	reduced χ^2	dof
12172038b	58835.6554	$0.47316^{+0.00400}_{-0.00398}$	$80.4^{+14.9}_{-11.1}$	$3.8192^{+0.0392}_{-0.0409}$	$1969.8^{+73.6}_{-70.8}$	0.1	1.01	286
12172039	58836.7168	$0.44177^{+0.00276}_{-0.00275}$	$144.0^{+46.6}_{-29.3}$	$3.6867^{+0.0459}_{-0.0496}$	$2272.4^{+69.5}_{-71.0}$	0.1	1.38	322
12172040	58837.6459	0.44314 ± 0.00250	$108.7^{+23.0}_{-16.7}$	$3.7566^{+0.0389}_{-0.0409}$	$2263.3^{+59.0}_{-57.8}$	0.1	1.40	335
12172041	58839.6383	$0.42725^{+0.00810}_{-0.00997}$	$170.6^{+12.2}_{-90.3}$	$3.619^{+0.128}_{-0.154}$	$2482^{+181.3}_{-658}$	0.1	1.22	235
12172042	58840.6992	$0.42024^{+0.00358}_{-0.00357}$	$121.1^{+34.2}_{-22.5}$	$3.6938^{+0.0459}_{-0.0492}$	$2484.5^{+91.8}_{-89.2}$	$0.1590^{+0.0183}_{-0.0182}$	1.52	315
12172043a	58841.6469	$0.43116^{+0.00408}_{-0.00406}$	$115.5^{+25.1}_{-18.1}$	$3.7353^{+0.0404}_{-0.0422}$	$2243.2^{+97.4}_{-93.4}$	0.1	1.12	257
12172043b	58841.7734	$0.42350^{+0.00355}_{-0.00354}$	$142.9^{+34.0}_{-23.7}$	$3.7449^{+0.0413}_{-0.0437}$	$2050.3^{+80.6}_{-78.0}$	0.1	1.54	276
12172044a	58842.6917	$0.42046^{+0.00353}_{-0.00350}$	$140.6^{+37.6}_{-25.7}$	$3.6752^{+0.0425}_{-0.0447}$	$2384.6^{+94.4}_{-91.8}$	0.1	1.29	275
12172044b	58842.7578	$0.42311^{+0.00392}_{-0.00391}$	$141.2^{+38.3}_{-26.0}$	$3.6794^{+0.0429}_{-0.0451}$	$2327.8^{+101.3}_{-97.8}$	0.1	1.14	262
12172045a	58843.699	$0.40695^{+0.00354}_{-0.00357}$	$66.54^{+13.16}_{-9.79}$	$3.6517^{+0.0412}_{-0.0430}$	$3940^{+159.1}_{-151}$	0.1	1.57	273
12172045b	58843.7645	$0.41042^{+0.00458}_{-0.00456}$	$89.1^{+17.2}_{-12.8}$	$3.7159^{+0.0409}_{-0.0426}$	$2931^{+150.8}_{-143}$	0.1	1.33	244
12172046a	58844.289	0.42936 ± 0.00400	$115.9^{+24.9}_{-18.0}$	$3.7737^{+0.0422}_{-0.0442}$	$2009.0^{+86.3}_{-82.3}$	0.1	1.23	268
12172046b	58844.3522	$0.43443^{+0.00399}_{-0.00397}$	$108.4^{+22.6}_{-16.4}$	$3.7771^{+0.0416}_{-0.0435}$	$2013.6^{+84.3}_{-80.8}$	0.1	1.09	268
12172047	58845.8187	0.40029 ± 0.00337	$103.5^{+27.1}_{-18.1}$	$3.7250^{+0.0517}_{-0.0552}$	$2710^{+107.3}_{-103}$	0.1	1.26	272
12172048a	58846.8847	$0.40890^{+0.00394}_{-0.00392}$	$114.7^{+26.8}_{-19.3}$	$3.7236^{+0.0444}_{-0.0459}$	$2411^{+108.1}_{-104}$	0.1	1.26	249
12172048b	58846.9539	$0.40036^{+0.00958}_{-0.00945}$	$123.1^{+28.7}_{-20.7}$	$3.7226^{+0.0489}_{-0.0503}$	$2438^{+277.9}_{-248}$	0.1	1.00	168
12172049a	58847.7398	$0.39681^{+0.00555}_{-0.00548}$	$98.7^{+21.0}_{-15.5}$	$3.7010^{+0.0427}_{-0.0443}$	$2830^{+171.3}_{-161}$	$0.1255^{+0.0274}_{-0.0272}$	1.38	236
12172049b	58847.8106	$0.40229^{+0.00477}_{-0.00473}$	$105.9^{+22.4}_{-16.6}$	$3.7271^{+0.0421}_{-0.0435}$	$2501^{+127.3}_{-121}$	$0.1340^{+0.0244}_{-0.0243}$	1.03	256
12172050	58848.883	$0.39490^{+0.01026}_{-0.00998}$	$142.3^{+251.5}_{-64.7}$	$3.693^{+0.124}_{-0.138}$	$2401^{+283.8}_{-287}$	$0.1476^{+0.0541}_{-0.0534}$	0.970	174
12172052	58850.2593	$0.40587^{+0.00483}_{-0.00478}$	$121.7^{+25.9}_{-18.9}$	$3.7388^{+0.0418}_{-0.0434}$	$2220^{+112.8}_{-107}$	$0.1250^{+0.0249}_{-0.0247}$	1.31	251
12172053	58851.254	$0.40075^{+0.00531}_{-0.00524}$	$152.7^{+-27.5}_{-27.5}$	$3.6968^{+0.0450}_{-0.0473}$	$2165^{+124.8}_{-119}$	$0.0193^{+0.0704}_{--0.0977}$	0.144	1.20
12172054	58852.4495	$0.37949^{+0.00482}_{-0.00477}$	$150.5^{+42.5}_{-28.3}$	$3.6319^{+0.0463}_{-0.0490}$	$2767^{+157.6}_{-150}$	$0.1057^{+0.0233}_{-0.0231}$	1.31	236
12172055	58853.3848	$0.37969^{+0.00570}_{-0.00562}$	$119.6^{+26.1}_{-18.9}$	$3.6892^{+0.0446}_{-0.0464}$	$2696^{+177.1}_{-166}$	$0.1276^{+0.0302}_{-0.0300}$	1.06	223
12172056	58854.315	$0.37282^{+0.00361}_{-0.00358}$	$112.9^{+25.2}_{-17.9}$	$3.6856^{+0.0451}_{-0.0474}$	$2910^{+124.3}_{-119}$	$0.1437^{+0.0190}_{-0.0188}$	1.41	267
12172057	58855.643	$0.38526^{+0.00458}_{-0.00454}$	$104.6^{+24.0}_{-16.9}$	$3.7094^{+0.0473}_{-0.0499}$	$2550^{+131.9}_{-125}$	$0.1456^{+0.0238}_{-0.0236}$	1.30	255
12172058	58856.5709	$0.36603^{+0.00317}_{-0.00316}$	$89.6^{+17.1}_{-12.7}$	$3.6687^{+0.0427}_{-0.0446}$	$3465^{+133.8}_{-129}$	$0.1214^{+0.0155}_{-0.0154}$	1.46	269
12172059a	58857.0981	$0.35184^{+0.00466}_{-0.00461}$	$116.7^{+25.8}_{-18.6}$	$3.6204^{+0.0435}_{-0.0455}$	$3446^{+203.8}_{-192}$	$0.1793^{+0.0266}_{-0.0264}$	1.36	229
12172059b	58857.1742	$0.37271^{+0.00505}_{-0.00500}$	$114.9^{+25.2}_{-18.2}$	$3.6651^{+0.0434}_{-0.0452}$	$2809^{+166.1}_{-156}$	$0.1705^{+0.0291}_{-0.0288}$	1.19	236
12172060a	58858.426	$0.34663^{+0.00488}_{-0.00482}$	$103.4^{+24.7}_{-17.4}$	$3.6072^{+0.0467}_{-0.0487}$	$3589^{+218.8}_{-206}$	$0.3843^{+0.0348}_{-0.0344}$	1.29	251
12172060b	58858.4916	$0.36263^{+0.00565}_{-0.00557}$	$102.9^{+25.0}_{-17.5}$	$3.6349^{+0.0472}_{-0.0493}$	$3140^{+210.2}_{-197}$	$0.3391^{+0.0377}_{-0.0373}$	1.30	249
12172064	58864.6897	$0.15640^{+0.00944}_{-0.00867}$	$159.2^{+96.3}_{-47.2}$	$3.139^{+0.107}_{-0.113}$	29120^{+9808}_{-7390}	$1.801^{+0.239}_{-0.203}$	1.09	128
12172066	58866.6131	$0.14375^{+0.00775}_{-0.00464}$	$221.0^{+46.3}_{-73.4}$	$3.01^{+0.10}_{-3.01}$	36210^{+6481}_{-8140}	$1.888^{+0.197}_{-0.186}$	1.07	170

[a] ObsIDs containing letters are observations that have been split into multiple GTIs.

[b] When the L_c/L_d parameter could not be contrained by the data, it was fixed at the default value of 0.1.

APPENDIX C: EXAMPLE BROAD-BAND SPECTRA

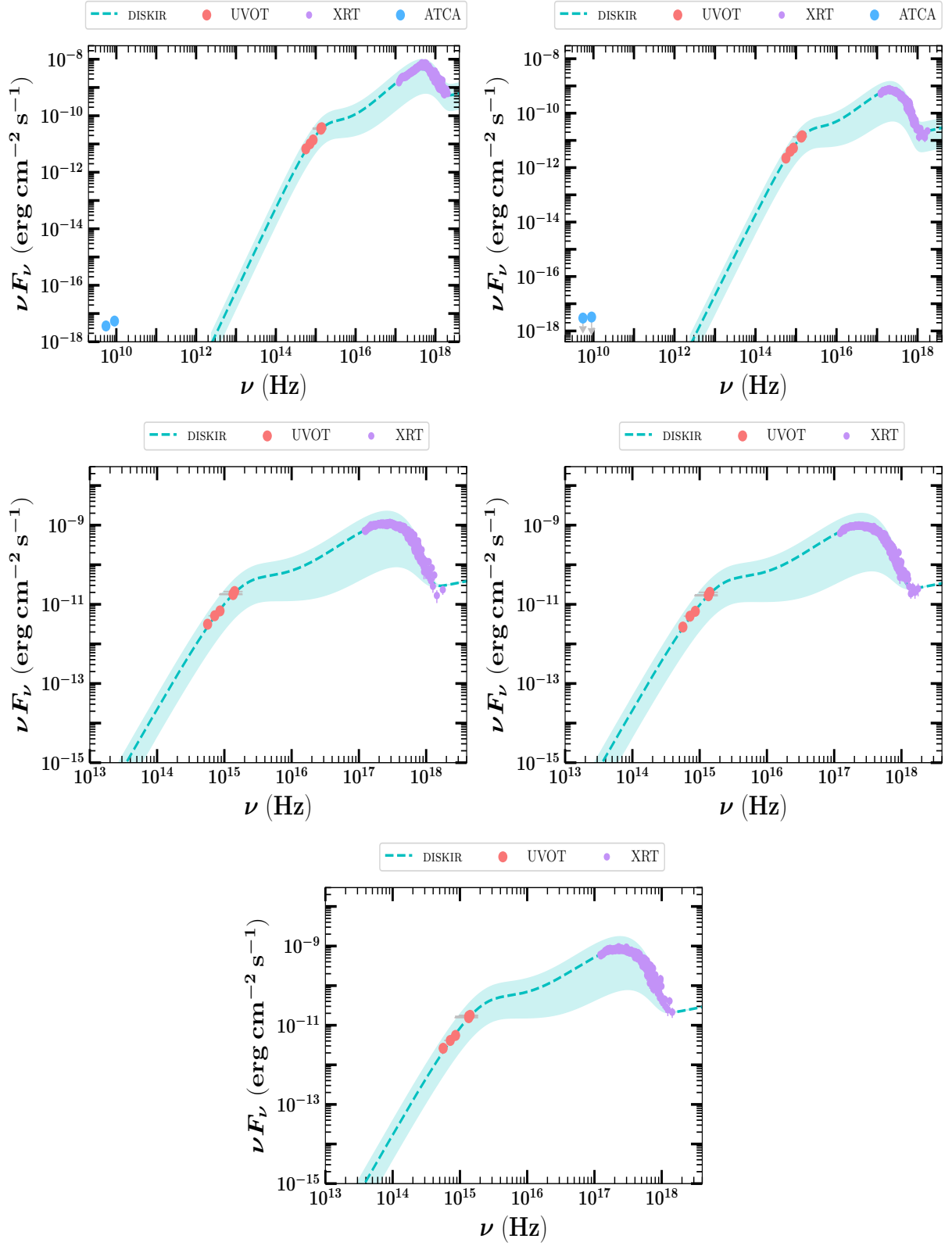This paper has been typeset from a TeX/LaTeX file prepared by the author.

Figure C1. Example broad-band SEDs quasi-simultaneous (within at most 10hrs of each other) with the *(top panel)* two epochs in which ATCA data were taken, and *(middle and bottom panels)* and three epochs in which Gemini/GMOS data were taken. *Swift*/XRT, *Swift*/UVOT, and ATCA (5.5 and 9 GHZ) data are shown as the purple, red, blue circular data points, respectively. The best-fit `diskir` model (dashed cyan line) and 1σ confidence interval on the fit (shaded cyan region) are also displayed in each SED.